REVIEW ARTICLE

Vanadium-Based Cathode Materials for Rechargeable Multivalent Batteries: Challenges and Opportunities

Han Tang[1] · Zhuo Peng[1] · Lu Wu[1] · Fangyu Xiong[1] · Cunyuan Pei[1] · Qinyou An[1] · Liqiang Mai[1]

Abstract

Due to the large reserves, low cost, high security and high energy density, rechargeable multivalent batteries have attracted extensive research enthusiasm for a long time. Multivalent batteries are also supposed as the potential candidates to Li-ion batteries in portable electronic devices and large-scale energy storage units. Unfortunately, most commercial cathode materials in Li-ion batteries cannot be applied in multivalent batteries because of the intensive polarization problem of multivalent intercalated ions (Mg^{2+}, Zn^{2+}, Al^{3+}). Choosing and synthesizing the appropriate cathode materials are the main issues in overcoming the intensive polarization problem. Vanadium-based materials often possess many kinds of oxidation states because of the mutable vanadium element, which can facilitate achieving local electroneutrality and relieve the polarization problem of multivalent ions. In this review, we summarize the researches about the vanadium-based cathode materials for multivalent batteries and highlight the intercalation mechanism of multivalent ions to vanadium-based materials. In addition, different kinds of optimizing strategies are extracted from the literatures. On the basis of our review, progresses and future challenges of vanadium-based cathode materials in rechargeable multivalent batteries are more explicit.

1 Introduction

Conventional combustion of fossil fuels is still the main portion of the energy supply methods in the world, although these non-renewable resources are very limited and difficult to sustain for many years because of the increasing energy consumption in the future [1–8]. In addition, carbon dioxide and other undesirable greenhouse pollutants promote the researchers to find green, economic and efficient renewable energy sources [9–11]. Solar energy, wind energy, tidal energy, geothermal energy and other kinds of renewable green energies are potential alternatives to substitute the conventional fossil

fuels [12–16]. In this regard, sustainable stationary electrical energy storage devices (EESDs) are required to reliably and efficiently store and transmit the electrical energy generated from the intermittent renewable sources [8, 17–19]. Although various technological innovations and scientific breakthroughs have been reported in recent years, the current EESDs still cannot satisfy the requirement in load leveling and power regulation [20–27]. Various battery technologies, such as lead–acid batteries, Ni–Cd batteries, Na–S batteries, vanadium redox flow batteries and Li-ion batteries, have been researched for a long time and applied partly in the EESDs or portable electronic devices, but all of these battery technologies have corresponding weaknesses [26–39]. Lead–acid batteries and Ni–Cd batteries are environmental hazards and suffer low energy density. Memory effect (when batteries charge and discharge many times incompletely, the batteries will generate a secondary discharge platform and the discharge capacity will decrease) is also a nonnegligible disadvantage in practical application [28, 30–33]. Na–S batteries require high operating temperature and suffer the safety problem of sodium metal [26, 27]. Vanadium redox flow batteries are

✉ Qinyou An
anqinyou86@whut.edu.cn

✉ Liqiang Mai
mlq518@whut.edu.cn

1 State Key Laboratory of Advanced Technology for Materials Synthesis and Processing, International School of Materials Science and Engineering, Wuhan University of Technology, Wuhan 430070, China

often costly, and maintenance charge is very high because the V_2O_5 phase will separate out in high temperature which might destroy the battery [34–36]. Li-ion batteries have acquired extensive attention in recent years and were applied in smart grids, hybrid electric vehicles, personal electric devices and electric vehicles successfully [37–39]. However, the further development of Li-ion batteries is still limited by resource scarcity, high prices, safety issues and energy density problem [40–42]. On the other hand, carbon-based anode materials with low capacity severely limited the energy density progress in Li-ion batteries [43, 44]. Rechargeable multivalent batteries (magnesium, zinc, aluminum batteries) tend to increase the energy density based on high-capacity multivalent metals which are used as anode materials directly (Table 1) [45]. In addition, because the multivalent cations could transfer two or three electrons per ion, multivalent cations could deliver higher capacity compared with Li^+ ions when intercalated into cathode materials if similar numbers of intercalant sites are occupied [45]. Compared with Li^+ ions intercalation cathode materials, the cathode materials that multivalent cations can intercalate are relatively unexplored and the literatures reported about the rechargeable multivalent batteries are also insufficient. Thus, there still are large development space and great application potential for multivalent batteries in the future [45–50].

Rechargeable magnesium batteries (RMBs) have received extensive attention in these years and are identified as one of the most promising candidates to Li-ion batteries in large-scale energy storage units and full electric vehicles [45–48]. Magnesium metal possesses a high gravimetric capacity of 2205 mAh g^{-1} and high volumetric capacity of 3833 mAh cm^{-3} with large reserves in the crust of earth [51]. Moreover, magnesium is safer and cheaper than lithium (Table 1). Two-dimensional deposition performance (Mg^{2+} ions deposit uniformly on anode interface and prefer non-dendrite type deposition in charge and discharge process) makes it feasible to use magnesium metal as anode material directly without generation of one-dimensional dendritic crystal which might impair separator film and result in the short circuit of battery [52, 53]. Mg^{2+} ions also have similar ionic radius of about 0.72 Å compared with the 0.76 Å of Li^+ ions [54]. But intensive electric density of Mg^{2+} ions

will result in the strong polarization effect and sluggish diffusion process in cathode materials [55]. The polarization problem comes from the large charge density of multivalent cations which might attract anions in the crystal lattice and break the local electroneutrality. When the local electroneutrality is destroyed severely, the crystal lattice will collapse and the electrochemical performance will suffer depravation. On the other hand, a rise in charge density will also increase the transfer impedance of cations and deteriorate the rate property of materials. Most commercial cathode materials in state-of-the-art Li-ion batteries exhibit poor rate performance and low capacity when applied in RMBs, due to the sluggish dynamics of Mg^{2+} ions [56]. Furthermore, passivation layer might appear on Mg metal surface in commonly nonaqueous polar organic solvents-based electrolyte [57]. Unlike the solid electrolyte interphase (SEI) in Li-ion battery, the passivation on Mg metal surface is ionic insulators which will prevent further reaction process in RMBs [56]. From the above analysis, finding decent cathode materials that could sustain intensive electric density of Mg^{2+} ions to provide fast-diffusion channel, and compatible electrolyte that could avoid the passivation problem and provide wide voltage window are the most urgent issues in the development of RMBs [45–48]. In 1990, Gregory et al. [58] reported that Mg^{2+} ions could be reversibly plated in the Grignard reagents (R-MgX, R = alkyl, X = Br, Cl). In 2000, Aurbach and co-workers methodically refined the Grignard reagents-based electrolyte to improve the magnesium anode stability and coulombic efficiency [59]. Ethereal solution of organomagnesium-chloride complexes ($Mg(AlCl_2BuEt)_2$ in THF, DCC) was developed, and RMBs prototype was designed seriously for the first time [59]. Based on the Chevrel phase Mo_6S_8 as cathode materials, the RMBs can deliver a stable capacity about 80 mAh g^{-1} and operate more than 2000 cycles with little capacity fading [59]. On the other hand, several other kinds of Chevrel phase ($M_xMo_6T_8$, M = metal, T = S, Se, Te) also exhibit the decent intercalation kinetics of Mg^{2+} ions and stable cycling performance [60–65]. Chevrel phase consists of Mo_6T_8 unit in which the cubes of T elements surround the Mo_6-octahedra clusters. The Mo_6T_8 unit will stack as the three-dimensional open frameworks based on face-sharing and corner-sharing, forming two different cavities for cations insertion. The negatively charged

Table 1 Comparative qualities of lithium, magnesium, zinc and aluminum

Parameter	Lithium	Magnesium	Zinc	Aluminum
Cationic radius (Å)	0.76	0.72	0.74	0.54
Atomic weight (g mol^{-1})	6.9	24.3	65.41	27
E (V vs. SHE)	− 3.04	− 2.37	− 0.76	− 1.66
Metallic capacity (mAh g^{-1})	3862	2205	819	2980
Metallic capacity (mAh cm^{-3})	2046	3833	5848	8046
Global yield (kg $year^{-1}$)	2.5×10^7	6.3×10^9	1.4×10^{10}	4×10^{10}
Price (USD kg^{-1})	~ 144	~ 2.7	~ 3.4	~ 1.4

frameworks and weak electrostatic interaction, optimize the Mg^{2+} ions mobility and reduce the diffusion barrier [47, 54]. In crystal structure of Mo_6S_8, eight chalcogenides surround the Mo_6 octahedral clusters with metallic bonds, which can regulate the electron density quickly and tolerate the intensity polarization effect. Thus, when Mg^{2+} ions diffuse in the Chevrel phase-based materials, polarization charge will redistribute rapidly and local electroneutrality will be retained relatively [47, 54]. Although the Chevrel phase-based materials possess the stable cycling performance and excellent dynamics property of Mg^{2+} ions, the poor specific capacity (~ 80 mAh g^{-1}) and low operating voltage (~ 1.1 V vs. Mg/Mg^{2+}) still limit the further development of Chevrel phase-based materials in RMBs [63]. Many kinds of materials, such as transition metal chalcogenides and oxides, polyanions compounds, NASICONs, borates compounds, prussian blue analogues, spinel-related materials and organic compounds, all exhibit unsatisfactory electrochemical property in RMBs [66–76]. Therefore, finding appropriate cathode materials that possess good rate performance and high capacity with high operating voltage is a great challenge in RMBs.

The electrolytes used in secondary batteries are mostly nonaqueous organic solvents, which have broad voltage window, and usually could achieve high energy density [77]. However, most organic solvents are toxic and flammable, resulting in serious safety problems in application. Besides, using nonaqueous electrolyte requires completely no-water production environment, which greatly raises the cost. These issues restrict their application in large-scale energy storage. Therefore, the aqueous electrolyte is a quite charming choice for researchers. Replacing organic electrolyte with aqueous electrolyte could further decrease the cost and improve safety. Aqueous electrolyte also possesses much higher electrical conductivity, compared with organic electrolyte. Zinc has low equilibrium potential, and high over potential of hydrogen evolution [78]. It has the lowest standard potential among all the metals that can reversibly deposit/dissolve in water-based solutions. Besides, the zinc metal has abundant resources, and is cost-effective and stable (Table 1). Thus, the aqueous rechargeable zinc batteries (RZBs) utilizing Zn metal anode and water-based electrolytes have broad prospects for large-scale energy storage. In 1991, Mclarnon and Cairns [79] first proposed the multivalent ion storage of α-MnO$_2$, and expanded the application of Zn metal anode to mild electrolyte systems. The α-MnO$_2$ owns large tunnels, in which the Zn^{2+} ions could reversibly insert/extract. The studies of RZBs are mostly focusing on the cathode materials. There are only a few kinds of cathode materials for RZBs that have been extensively investigated at present: polymorphous of MnO$_2$ [80–83] and Prussian blue analogues [84, 85]. Those materials suffer some defects, for instance, the rate performance of manganese dioxide is not satisfactory, and the Prussian blue analogue delivers low capacity. In recent years, some vanadium-based materials have been reported and part of them exhibit excellent electrochemical performance in aqueous RZBs system.

Among multivalent battery systems, rechargeable aluminum batteries (RABs) possess unique advantages. Aluminum is the most abundant metal in the earth's crust, and as one of the highest multivalent charge carriers (Al^{3+}), it can provide high volumetric capacity and gravimetric capacity of 8046 mAh cm^{-3} and 2980 mAh g^{-1}, respectively [49, 86–88]. Additionally, aluminum metal is also much cheaper than other metals (Table 1). Safety and availability are also important factors that make RABs a promising candidates. Despite these advantages of RABs system, the practical application of RABs has faced many problems, one of which is electrolyte. As we know, the electrolyte is an important component in battery system. In early times, Al metal used as anode could date back to 1857 when the dilute H_2SO_4 solution was adopted in electrolyte [87]. In recent years, the anatase TiO$_2$ with 1.0 M Al(NO$_3$)$_3$ aqueous electrolyte performed well, but there are some problems that remain in this aqueous system [89]. For instance, different pH values will result in different kinds of cluster formations (Al^{3+}, AlO_2^-, and Al_2O_3), which limits the development of the high energy density RABs system [49]. For these reasons, the aqueous system still has no significant breakthrough. Investigation of nonaqueous electrolytes has drawn more attention because of the stable performance and higher efficiency. Moreover, the nonaqueous electrolytes can provide wider voltage windows compared to aqueous electrolytes. At present, the improvement in organic electrolytes in RABs is still insufficient, and we need to explore a more suitable and high-performance organic electrolyte. Cathode material is another important parameter for RABs. Unlike monovalent metal-based batteries (Li$^+$, Na$^+$), the RABs have the highest requirement for cathode materials because Al^{3+} ions have strong polarization effect and the ionic group chloroaluminate anion ($AlCl_4^-$, another kind of inserted species in RABs) is too large to intercalate into cathode materials, which leads to the lower stability and capacity of cathode materials. In the research process of the cathode materials applied in RABs, the carbon-based materials play important roles, in which the most noticeable material is the graphitic foam. It achieved 7500 cycles life at 4000 mA g^{-1} and the coulombic efficiency could remain at 97%, which is an excellent electrochemical performance in the reported materials of RABs [90]. On the other hand, researches of large-sized few-layered graphene and defect-free advanced graphene aerogel in the RABs have been published and also obtained good results [91, 92]. However, the low discharge capacity of graphite-type materials could not meet the demand for high energy density. The transition metal sulfides, such as FeS$_2$, Ni$_3$S$_2$

and CuS, have overcome the limitation of the low capacity [93–95]. But these kinds of materials might suffer the dissolution problem in acidic electrolytes, which leads to the seriously decay of capacity [96].

Considering the dilemma of multivalent batteries, vanadium-based compounds as cathode materials have attracted much attention [97, 98]. Vanadium-based compounds have been researched as potential cathode materials in various battery systems for about 40 years and part of which have got practical application [99]. Diverse vanadium oxide structures are generated because of the facile distortion of V–O octahedra and rich chemical valences (V^{2+}, V^{3+}, V^{4+}, V^{5+}). The multiple oxidation states of the vanadium provide broader variation range and higher specific capacity when multivalent cations intercalate into the vanadium-based materials. Vanadium also can facilitate achieving local electroneutrality by changing two or more oxidation states to stabilize the crystal structure and optimize the multivalent cations diffusion process. On the other hand, the occupied extent of d-orbitals in element will impact the magnitude of the structural change. In octahedral environment, only a small volume change will occur when nonbonding orbitals are filled, but if antibonding orbitals are filled, the volume will suffer a huge extension [100, 101]. Vanadium as one of the early transition metals has several unoccupied nonbonding orbitals, unlike the late transition metals, in which one or more antibonding orbitals are often filled [100, 101]. Thus, vanadium-based compounds could be considered as qualified candidates for cathode materials in multivalent batteries.

In this review, vanadium-based compounds applied in RMBs, RZBs and RABs are presented, respectively (Table 2). Not only electrochemical performances of various vanadium-based compounds are recommended, but the fundamental science about the complex intercalation reactions between multivalent cations and materials are also deeply studied. Different structural evolutions during multivalent cation insertion process are discussed by multiple characterization techniques results. Understanding the electrochemical process sufficiently in multivalent batteries is the basic step in improving the electrochemical performance of vanadium-based compounds. Moreover, special objective factors in materials or electrolytes, such as water molecules, which might affect multivalent cations intercalation process, are systematically studied with a variety of research results. Different optimized designs in vanadium-based compounds, such as carbon composites, pre-intercalation, doping and amorphization, are exhibited in this review. In addition, the optimization performances are compared, which has guiding significance for the future development of the vanadium-based compounds. Compared with the commercial cathode materials in state-of-the-art Li-ion batteries, vanadium-based compounds in multivalent batteries still have the great gap, but the enormous potential of this new battery system constantly stimulates the researchers to overcome the continuous challenges.

2 Vanadium-Based Compounds for Rechargeable Magnesium Battery System

RMBs hold great promises for high energy density, safety, and low-price energy storage devices. Dendritic-free deposition property and high deposition/dissolution efficiency of Mg anode make the RMBs more prospective. Sulfide materials have been investigated deeply in RMBs because Mg^{2+} ions could diffuse steadily in this kind of materials. Low discharge voltage and energy density limit the further development of sulfide materials. Various vanadium-based materials have been researched in RMBs for a long time and some of them exhibit decent reactivity of Mg^{2+} ions storage. Mg^{2+} ions often strongly interact with framework lattice because of the high charge/radius ratio, but vanadium-based materials possess facile distortion structure and large cations storage cavities, which can lower diffusion barrier of Mg^{2+} ions and provide more reactive sites. At present, the reaction mechanism of some vanadium oxides, such as V_2O_5, has been investigated deeply. But the electrochemical performance of vanadium oxides is dissatisfactory. Many improvement methods have been proposed in these years, and the Mg^{2+} ions storage performance of vanadium oxides has been much promoted. Other kinds of vanadium-based materials, such as phosphate compounds, hydrous vanadate compounds and calcium ferrite type materials, exhibit decent Mg^{2+} ions storage property and the reaction mechanism will be discussed in the following content.

2.1 Vanadium Oxides

V_2O_5 is a typical layered material that different V–O polyhedron constitute the layered framework. Different phases will appear and the layered structure will change when cations intercalate into the framework. In Li-ion batteries, V_2O_5 could provide large specific capacity and high working voltage. Thus, V_2O_5 has received much attention in the energy storage materials [45, 46, 102]. In 1993, Novak et al. [103, 104] tested the conventional orthorhombic V_2O_5 electrode in $Mg(ClO_4)_2$/AN electrolyte, and specific capacity of 170 mAh g^{-1} was measured in the first cycle. But the capacity decayed drastically in the further cycling process, which was attributed to the dissolution of V_2O_5 in the electrolyte. Passerini et al. reported that V_2O_5 with high porosities and high surface areas might attain a high specific energy of about 1200 W h kg^{-1} [105]. This work indicated that V_2O_5 is a potential material in RMBs.

Table 2 The electrochemical performance of vanadium-based cathode materials for rechargeable multivalent batteries

Material	Electrolyte	Counter electrode	Operation range (V)	Initial capacity (mAh g^{-1})	Current density (mA g^{-1})	Capacity retention (mAh g^{-1})	References
V_2O_5	$Mg(ClO_4)_2$/AN	Mg	1.0–2.5 V versus Mg/Mg^{2+}	~ 170	–	–	[103]
V_2O_5 thin-film	$Mg(ClO_4)_2$/AN	AC	2.1–3.0 V versus Mg/Mg^{2+}	~ 180	–	~ 150 after 36 cycles	[51]
Mg-V_2O_5	$Mg(ClO_4)_2$/AN	Sn	0.0–2.0 V versus Mg/Mg^{2+}	~ 160	30	~ 120 after 50 cycles	[109]
V_2O_5/C	$Mg(ClO_4)_2$/AN	Mg	2.0–3.4 V versus Mg/Mg^{2+}	~ 325	17,000	~ 290 after 35 cycles	[111]
RFC/V_2O_5	$[Mg_2(\mu Cl)_2(DME)_4][AlCl_4]_2$/DME	Mg	0.5–2.8 V versus Mg/Mg^{2+}	~ 120	320	~ 80 after 100 cycles	[113]
V_2O_5/GO	$Mg(TFSI)_2$/AN	AC	1.6–3.4 V versus Mg/Mg^{2+}	~ 280	100	~ 210 30 cycles	[114]
V_2O_5/GO	$Mg(AlCl_2EtBu)_2$/THF	Mg	1.0–2.8 V versus Mg/Mg^{2+}	~ 178	58	~ 140 after 20 cycles	[115]
S-V_2O_5	$Mg(ClO_4)_2$/H_2O/PC	Pt	0.9–2.4 V versus Mg/Mg^{2+}	~ 300	60	~ 300 after 3 cycles	[117]
V_2O_5-P_2O_5	$Mg(ClO_4)_2$/AN	Mg	1.1–3.4 V versus Mg/Mg^{2+}	~ 120	65	–	[118]
V_2O_5-PEO	$Mg(ClO_4)_2$/AN	Mg	1.0–3.0 V versus Mg/Mg^{2+}	~ 130	10	~ 90 after 35 cycles	[124]
VO_2(B)	$Mg(ClO_4)_2$/AN	AC	1.6–3.0 V versus Mg/Mg^{2+}	~ 400	50	~ 200 after 60 cycles	[127]
$VO_{2.37}$	$Mg(AlBu_2Cl_2)_2$/THF	Mg	0.2–1.6 V versus Mg/Mg^{2+}	~ 76	5	–	[130]
VO_x	$Mg(ClO_4)_2$/AN	Mg	1.5–3.5 V versus Mg/Mg^{2+}	~ 215	60	~ 150 after 20 cycles	[131]
NaV_3O_8	$MgCl_2$/$AlCl_3$/EMIC	Al	1.2–2.4 V versus Mg/Mg^{2+}	~ 110	–	–	[103]
$Mg(V_3O_8)_2$	$MgCl_2$/$AlCl_3$/EMIC	Al	1.2–2.4 V versus Mg/Mg^{2+}	~ 155	–	~ 60 after 50 cycles	[103]
$NaV_3O_8 \cdot 1.69H_2O$	$AlCl_3$-$(PhMgCl)_2$/THF	Mg	0.0–2.0 V versus Mg/Mg^{2+}	~ 60	50	~ 40 after 100 cycles	[135]
NaV_6O_{15}	$Mg(ClO_4)_2$/AN	Mg	0.1–3.0 V versus Mg/Mg^{2+}	~ 90	0.05	0 after 25 cycles	[136]
$Li_3V_2(PO_4)_3$	$Mg(TFSI)_2$/AN	Mg	1.5–3.8 V versus Mg/Mg^{2+}	~ 197	10	~ 197 after 5 cycles	[144]
$Na_3V_2(PO_4)_3$	$Mg(TFSI)_2$/DME	Mg	0.5–2.2 V versus Mg/Mg^{2+}	~ 97	10	–	[150]
$Na_3V_2(PO_4)_3$/C	$Mg(TFSI)_2$/AN	AC	2.0–3.0 V versus Mg/Mg^{2+}	~ 88.8	20	~ 80 after 100 cycles	[152]
$Mo_{2.48}VO_{9.93}$	$Mg(TFSI)_2$/AN	AC	1.7–3.3 V versus Mg/Mg^{2+}	~ 379	2	~ 235 after 15 cycles	[156]
V_2MoO_8	$AlCl_3$-$(PhMgCl)_2$/THF	Mg	0.4–2.4 V versus Mg/Mg^{2+}	~ 200	20	~ 60 after 1 cycles	[157]
VOCl	$(HMDS)_2$Mg/DEG/TEG	Mg	0.5–2.5 V versus Mg/Mg^{2+}	~ 160	10	~ 100 after 50 cycles	[161]
$Na_{0.25}V_{1.25}Ti_{0.75}O_4$	$Mg(CB_{11}H_{12})_2$/TEG	Mg	0.0–3.0 V versus Mg/Mg^{2+}	~ 80	5	~ 40 after 4 cycles	[164]
V_2O_5/GO	$Zn(CF_3SO_3)_2$/water	Zn	0.2–1.6 V versus Zn/Zn^{2+}	~ 230	6000	~ 210 after 900 cycles	[165]
V_2O_5/CFS	$Zn(TFSI)_2$/AN	Zn	0.3–1.5 V versus Zn/Zn^{2+}	~ 196	14.4	~ 170 after 120 cycles	[166]
$Zn_{0.25}V_2O_5 \cdot nH_2O$	$ZnSO_4$/water	Zn	0.5–1.4 V versus Zn/Zn^{2+}	~ 230	2400	~ 210 after 1000 cycles	[167]
$Na_{0.33}V_2O_5$	$Zn(CH_3F_3SO_3)_2$/water	Zn	0.2–1.6 V versus Zn/Zn^{2+}	~ 300	1000	~ 218 after 1000 cycles	[169]
$Zn_3V_2O_7(OH)_2 \cdot 2H_2O$	$ZnSO_4$/water	Zn	0.2–1.8 V versus Zn/Zn^{2+}	~ 150	200	101 after 300 cycles	[170]
LiV_3O_8	$ZnSO_4$/water	Zn	0.6–1.2 V versus Zn/Zn^{2+}	~ 70	133	~ 130 after 65 cycles	[171]
$H_2V_3O_8$	$Zn(CF_3SO_3)_2$/water	Zn	0.2–1.6 V versus Zn/Zn^{2+}	173.6	5000	136.1 after 1000 cycles	[173]
$Na_3V_2(PO_4)_3$	$Zn(CH_3COO)_2$/water	Zn	0.8–1.7 V versus Zn/Zn^{2+}	97	50	72 after 100 cycles	[177]
$Na_2TiV(PO_4)_3$	$ZnSO_4$/water	AC	0.9–1.5 V versus Zn/Zn^{2+}	55	128	52 after 10 cycles	[179]
VS_2	$ZnSO_4$/water	Zn	0.4–1.0 V versus Zn/Zn^{2+}	112.3	500	110.9 after 200 cycles	[180]
$V_{0.95}Al_{0.05}O_{1.52}(OH)_{0.77}$	$ZnSO_4$/water	Zn	0.2–1.13 V versus Zn/Zn^{2+}	156	15	105 after 50 cycles	[181]
V_2O_5 nanowires	1.1:1 $AlCl_3$:[EMIm]Cl	Al	0.02–2.5 V versus Al/Al^{3+}	305	125	273 after 20 cycles	[86]
V_2O_5/Ni	1.1:1 $AlCl_3$:[BMIm]Cl	Al	0.02–2.5 V versus Al/Al^{3+}	239	44.2	–	[184]
V_2O_5 nanowires	1.1:1 $AlCl_3$:[BMIm]Cl	Al	0.02–2.5 V versus Al/Al^{3+}	107	–	~ 40 after 10 cycles	[185]
V_2O_5/C	1:10:5 $AlCl_3$:dispropylsulfone:toluence	Al	0.1–2.5 V versus Al/Al^{3+}	60	44.2	~ 50 after 30 cycles	[186]
V_2O_5 nanowires	$(Al(OTF)_3)$/[BMIM]OTF	Al	0.02–3 V versus Al/Al^{3+}	87	10	~ 30 after 20 cycles	[189]
xero-V_2O_5	$AlCl_3$/water	AC	1.5–2.0 V versus Al/Al^{3+}	~ 110	60	~ 75 after 13 cycles	[191]
VO_2	1:1 $AlCl_3$:[BMIm]Cl	Al	0.01–0.9 V versus Al/Al^{3+}	165	50	116 after 100 cycles	[192]
Li_3VO_4/C	1.3:1 $AlCl_3$:[EMIm]Cl	Al	0.05–0.95 V versus Al/Al^{3+}	137	20	48 after 100 cycles	[195]
$Na_3V_2(PO_4)_3$	$AlCl_3$/water	Pt	1.9–2.4 V versus Al/Al^{3+}	~ 120	60	~ 60 after 20 cycles	[196]
V_2CT_x	1.3:1 $AlCl_3$:[EMIm]Cl	Al	0.1–1.8 V versus Al/Al^{3+}	335	10	~ 100 after 20 cycles	[199]
VS_4/rGO	1.3:1 $AlCl_3$:[EMIm]Cl	Al	0.1–2.0 V versus Al/Al^{3+}	~ 400	100	~ 90 after 100 cycles	[200]

To investigate the key issues of V_2O_5 in RMBs, many works about first-principle calculations based on density functional theory (DFT) have been carried out [106–108]. Firstly, the difference of Li and Mg atoms in adsorption and diffusion properties on single-layered and bulk V_2O_5 was studied [106]. From the result, binding energies of Li/Mg in bulk V_2O_5 (0.69 eV for Li and 2.20 eV for Mg) are smaller than those in single-layered V_2O_5 (3.28 eV for Li and 4.06 eV

for Mg). In addition, the single-layered V_2O_5 has more number of active sites that could adsorb cations. As for diffusion barrier, which links with the rate property, Li can diffuse faster in single-layered V_2O_5 (0.20 eV) than in bulk V_2O_5 (0.39 eV). However, the situation is different for Mg atom, its diffusion barriers in single-layered and bulk V_2O_5 are similar (1.36 eV for single-layered V_2O_5 and 1.40 eV for bulk V_2O_5) (Fig. 1a, b). The author simulated the charge density difference of Li/Mg atoms in single-layered and bulk V_2O_5 (Fig. 1c–f). The Mg–O bond length, unlike the Li–O bond, did not decrease much in the single-layered V_2O_5 compared with bulk V_2O_5, which might explain the enormous diffusion barrier of Mg atoms in single-layered V_2O_5. Zhou et al. [107] also discussed the crystalline V_2O_5 property by using first-principle calculations. They concluded that α-V_2O_5 has higher electronic conductivity compared with other V_2O_5 phases because of the small band gap. For diffusion rate, Mg atoms have much higher barrier (1.26 eV) than Li atoms in α-V_2O_5 (0.35 eV). Double-peak potential energy path of about 0.81 eV was also calculated in Mg atoms diffusion process which might account for the poor rate property of V_2O_5 in RMBs. From the elastic constants calculation results, the V_2O_5 structure will suffer shear distortion when Mg^{2+} ions intercalate into the interval site and phase transition will occur with no barrier. From the above calculation results, the diffusion of Mg^{2+} ions in V_2O_5 is sluggish. To solve this problem, some researchers found that the co-intercalation of H_2O and Mg^{2+} ions might improve the electrochemical performance of RMBs [108]. Gautam and co-workers discussed the Mg insertion voltage and phase transformation of Mg-H_2O-xerogel V_2O_5 in different electrolytic conditions [108]. They thought that intercalated Mg^{2+} ions and H_2O molecules located at V_2O_5 bilayers. In interlayer, each of Mg^{2+} ions was bonded with two O atoms from VO_x polyhedra and four O atoms from interlayered H_2O molecules (Fig. 1g). After DFT calculation, it can be concluded that the water content impacted the thermodynamic driving force of Mg^{2+} ions. In the electrolyte with high water content, Mg^{2+} ions can intercalate into V_2O_5 xerogel with high content and shuttle along with the water molecules. But in dry conditions, the intercalation of Mg^{2+} ions will decrease and water molecules might not shuttle with Mg^{2+} ions. More importantly, Mg^{2+} ions insertion voltage will increase with high-water-content electrolyte and phase behavior will become more diversified compared with superdry condition (Fig. 2a). Although the calculation results in these works might be different from the practical process, in considering temperature, electrolyte and crystallographic defects, the theoretical calculation is still a powerful assistant method to predict the electrochemical properties.

In actual conditions, intercalation process of Mg^{2+} ions in V_2O_5 is complicated. Many researchers have investigated the intercalation mechanism of $Mg^{2+}$ ions in different conditions [51, 109, 110]. Gershinsky et al. [51] researched Mg^{2+} ions intercalation process in thin-film V_2O_5 electrode completely by using electrochemical and spectroscopic analysis. In three-electrode system, active carbon clothes were used as counter and quasi-reference electrodes in 0.5 M $Mg(ClO_4)_2$/AN electrolyte. The redox reaction in charge and discharge process was ascertained by visual inspection, in which V_2O_5 went through the color changes [yellow (V^{5+}) to green (V^{4+}) in discharge process and reversed in charge process]. Energy dispersive spectrometer (EDS) patterns indicated the intercalation of Mg^{2+} ions (Fig. 2b). In galvanostatic charge and discharge process, V_2O_5 thin film could achieve the capacity of 150 mAh g^{-1} at 2.4 V (vs. Mg/Mg^{2+}) with 97% coulombic efficiency, corresponding to 0.5 mol Mg^{2+} ions intercalation per formula unit of V_2O_5. The layers of V_2O_5 are weakly bonded by van der Waals force, and the vanadium could change the oxidation state to provide electroneutrality when Mg^{2+} ions intercalated and diffused in the oxygen-terminated slabs. As long as the orthorhombic V_2O_5 can sustain the electronic polarization effect and layered expansion, the guest ions can be inserted into the material constantly. But compared with Li^+ ions intercalation process in the same measured system, over potential of Mg^{2+} ions insertion (700 mV) is larger than Li^+ ions (25 mV), indicating the slower kinetics of Mg^{2+} ions insertion process. On the other hand, there is multiple-step process in the magnesiation process, the different thermodynamics and properties in magnesiation process can be attributed to the different phase formations. Novak et al. [102] even postulated that there are ten different phase transition in Mg-V_2O_5 phase. Moreover, Gershinsky et al. [51] also found the change of layered distance and the randomization of bond in the structure from ex situ X-ray diffraction (XRD) pattern and Raman spectra (Fig. 2c, d). To investigate the insertion mechanism of Mg^{2+} ions more deeply, Tepavcevic et al. [109] enriched the bilayered V_2O_5 with Mg^{2+} ions via electrochemical synthesis method and assembled coin cell that Mg-V_2O_5 matched with nanocrystalline Sn in 1 M $Mg(ClO_4)_2$/AN electrolyte. In Mg^{2+} ions enrichment process, the capacity of 240 mAh g^{-1} was obtained when V_2O_5 countered with Mg metal (in $Mg(ClO_4)_2$/AN electrolyte) [109]. The process that Mg^{2+} ions intercalate into the bilayered structure was demonstrated by the X-ray absorption fine structure (XAFS), X-ray fluorescence (XRF), small-angle X-ray scattering (SAXS), X-ray photoelectron spectroscopy (XPS), and high-angle annular dark-field (HAADF) techniques. Three kinds of water are also found in bilayered Mg-V_2O_5. One of them is free water adsorbed in layer, and the second is bonded water in the layers linked by hydrogen bonds. The third type of water is the structural hydroxyl groups from the electrochemically synthesized Mg-V_2O_5. These kinds of water will maintain the large interlayered space to lubricate the solvated Mg^{2+} ions diffusion path and shield

or stabilize the divalent Mg^{2+} ions. Furthermore, discharged-state bilayered Mg-V_2O_5 was cycled with Sn anode. This full cell delivered an initial capacity about 160 mAh g^{-1} and decreased to 80 mAh g^{-1} after 20 cycles. After 50 cycles, the capacity recovered to 120 mAh g^{-1}, which was attributed to the nanocrystalline nature. Except electrochemical synthesis method, Lee et al. [110] also synthesized Mg-V_2O_5 ($Mg_{0.1}V_2O_5$) by using a sol–gel method in room temperature. This Mg-V_2O_5 exhibits good electrochemical performance and the high capacity of 300 mAh g^{-1} could be obtained. Moreover, different electrolytes also affect the electrochemical performance. From the experiment result, the CH_3CN related electrolyte is more compatible than carbonate-based solvents when linking to Mg^{2+} ions insertion process.

To improve the electrochemical performance of V_2O_5 in RMBs, many optimization methods, such as carbon coating, graphene recombination and micromorphology control,

were applied [111–113]. Imamura et al. [111] synthesized the V_2O_5/C composites from homogeneous suspension, which consist of vanadium pentoxide and acetylene black. They found out the most suitable weight ratio of V_2O_5 to carbon (3:1) and they also detected the stabilities of different current collectors (indium-tin oxide > stainless steel SUS304 net > nickel-foamed metal) in $Mg(ClO_4)_2$/AN electrolyte. High capacity of 600 mAh g^{-1} is obtained at 1 A g^{-1} for V_2O_5/C composites but the ordinary mixture of V_2O_5 gel and acetylene black only gets 150 mAh g^{-1} in the same condition. The V_2O_5/C composites increase the electronic conductivity and microscopic reaction areas. In this work, although the interlayer spacing change of V_2O_5 was discovered from ex situ XRD result, the detailed reaction mechanism is still unclear because the Mg rod is incompatible with the $Mg(ClO_4)_2$/AN electrolyte and the inductively coupled plasma (ICP) result is unable to explain the

Fig. 1 Energy barriers for **a** Li and **b** Mg atoms along the diffusion paths in single-layered and bulk V_2O_5. Isosurfaces of the charge density differences for **c** Li and **d** Mg located at the T site on the single-layered V_2O_5. Isosurfaces of the charge density differences for **e** Li and **f** Mg located at the T site on the bulk V_2O_5. Figure **a–f** reproduced with permission [106]. Copyright 2013, Royal Society of Chemistry, the structures of **g** the fully magnesiated ($x_{Mg} = 0.5$) and **h** the fully demagnesiated xerogel with one H_2O per formula unit of V_2O_5. A closer view of the Mg coordination environment in the xerogel is displayed within the green circles of **g**. Figure **g**, **h** reproduced with permission [108]. Copyright 2016, American Chemical Society
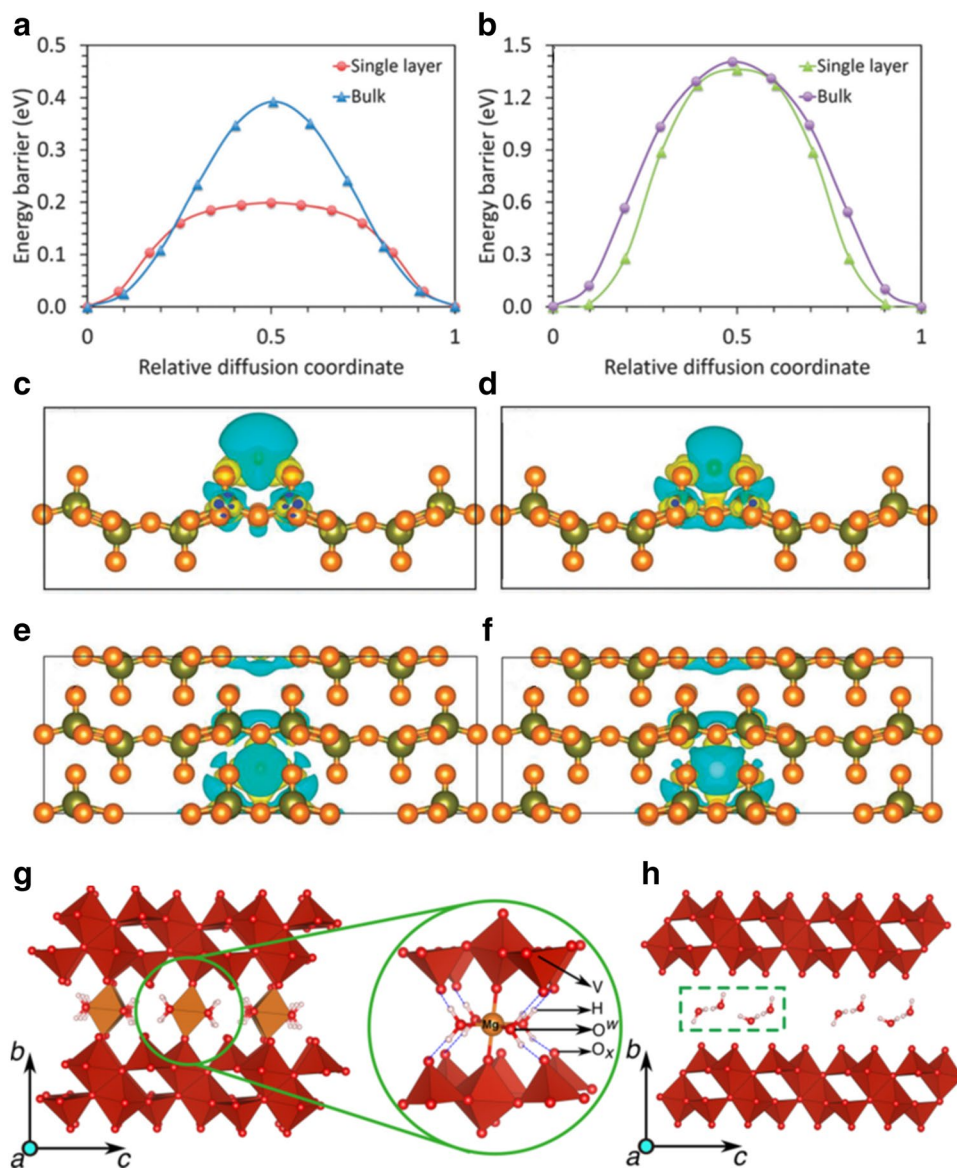
measured specific capacity. Except solid-state diffusion process of Mg^{2+} ions, pseudocapacitance might also exist in the cycling process of V_2O_5/C composites [112, 113]. Cheng et al. [113] synthesized the high dispersed V_2O_5 nanoclusters supported on porous carbon. This amorphous compound has the pseudocapacitive performance when cycling in 0.2 M $[Mg_2(\mu$-Cl$)_2$(DME)$_4][$AlCl$_4]_2$/DME electrolyte and the composites exhibit an outstanding rate performance. At the high current density of 640 mA g^{-1}, the composites could display the capacity of 100 mAh g^{-1}. After the analysis of electron microscopy, spectroscopy, and electrochemistry characterizations, there is no substantial solid-state Mg^{2+} ions diffusion process and the reversible chemical binding reaction in active surface of molecular nanoclusters dominates the cycling process. This work provides a viable approach to optimize the reaction kinetics in V_2O_5.

In addition, high-voltage as well as high-capacity RMBs was assembled based on "molecular storage mechanism" in this work. Generally, carbon composite could improve the electrical conductivity of materials and optimize the rate property of batteries. However, excess carbon content might reduce the energy density of batteries. Except V_2O_5/C composites, V_2O_5/GO composites also have been synthesized by many researchers [114, 115]. An et al. [114] synthesized nanowires/GO nanocomposites via freeze drying and annealing process. This V_2O_5/GO aerogel exhibits excellent electrochemical performance in Mg^{2+} ions storage. Except the special structure that graphene is convolved by V_2O_5 nanowires (Fig. 2e), the crystal water molecules in layers also play an important role in Mg^{2+} ions diffusion. When active carbon was used as counter and reference electrodes in Mg(TFSI)$_2$/AN electrolyte, high capacity at
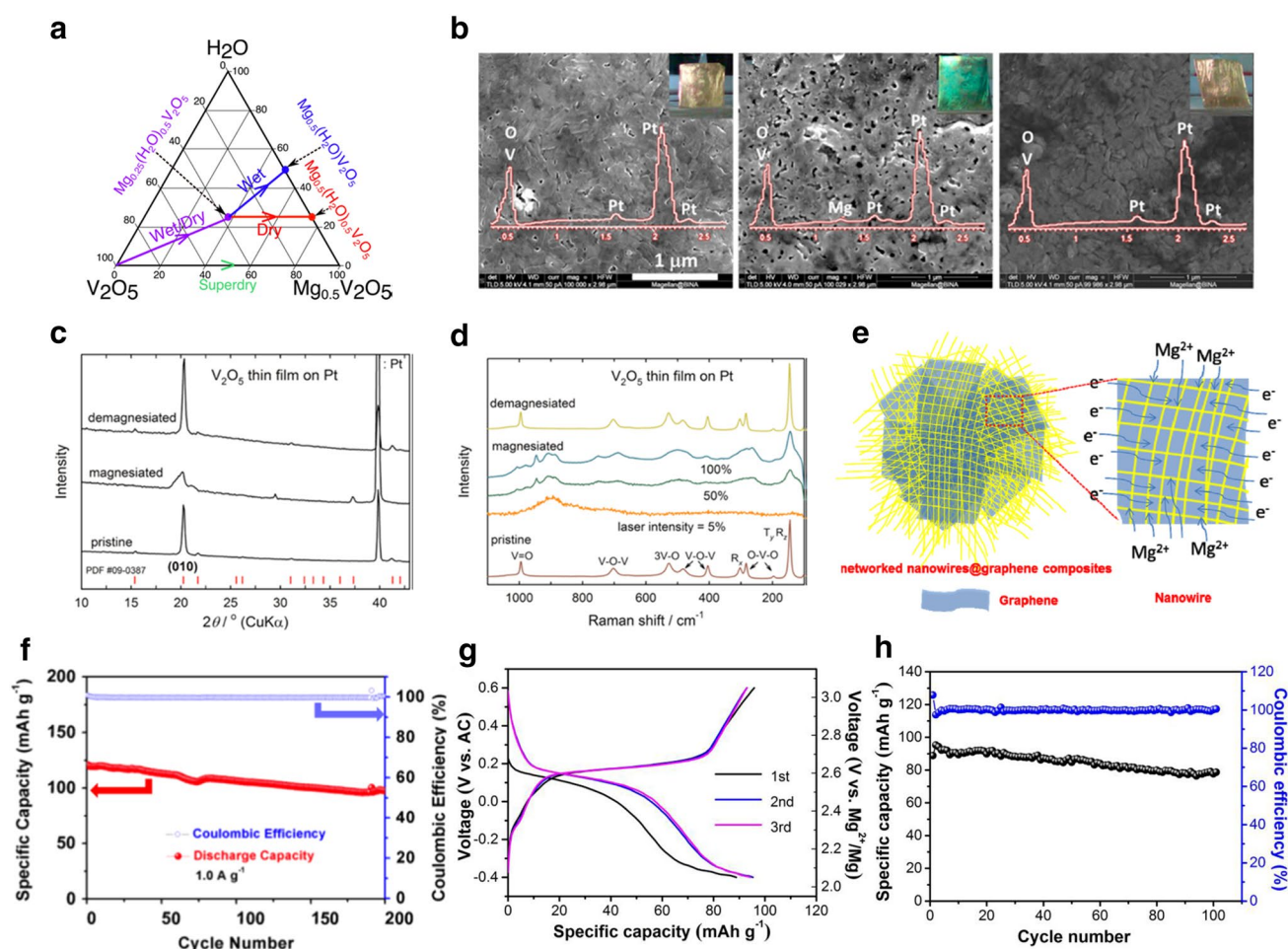

Fig. 2 **a** Ternary phase diagram of the Mg-(Xerogel)V$_2$O$_5$-H$_2$O system, which summarizes the possible equilibrium phases under different electrolyte conditions, reproduced with permission [108]. Copyright 2016, American Chemical Society. **b** HR-SEM images of the V$_2$O$_5$ thin-film electrodes: pristine, magnesiated (Mg$_{0.5}$V$_2$O$_5$), and demagnesiated in Mg(ClO$_4$)$_2$/AN solution. EDS patterns are presented in the images (overlapped), and visual photographs of the electrodes are presented in the insets. **c** XRD patterns and **d** Raman spectra of pristine, magnesiated (Mg$_{0.5}$V$_2$O$_5$), and demagnesiated V$_2$O$_5$ thin-film electrodes. Figure **b–d** reproduced with permission [51]. Copyright 2013, American Chemical Society, **e** schematic illustration and **f** cycling performance of the V$_2$O$_5$/GO nanocomposite at 1.0 A g^{-1}, reproduced with permission [114]. Copyright 2015, Elsevier, **g** galvanostatic charge–discharge voltage profiles and **h** cycling performance of the ED-NVP/C at 20 mA g^{-1}, reproduced with permission [152]. Copyright 2017, Wiley–VCH

around 280 mAh g^{-1} could be obtained at 100 mA g^{-1}. At high current density of 1.0 A g^{-1}, 81% capacity could remain after 200 cycles (Fig. 2f). This nanocomposite also exhibited the outstanding rate property and wide working temperature range. The authors further annealed nanocomposites to remove the crystal water molecules, but annealed nanocomposites exhibited a deteriorated electrochemical property. They concluded that the crystal water shielded the strong polarization effect of multivalent Mg^{2+} ions and reduced the diffusion barrier in insertion kinetics. When Mg^{2+} ions intercalate into the V$_2$O$_5$/GO aerogel, the dipole molecule (H$_2$O in crystal) will coordinate to Mg^{2+} ions as the solvation shell and transform Mg^{2+} ions into less polarized and solvated ions. In this solvation process, the dipole moments of multivalent Mg^{2+} ions will reduce and the strong polarization effect of Mg^{2+} ions will be shielded by crystal water molecules [114]. Du et al. [115] also synthesized orthorhombic V$_2$O$_5$/GO by using hydrothermal method in 200 °C followed by calcinating process. This composite is constituted of orthorhombic V$_2$O$_5$ microparticles wrapping around GO sheets. In 0.25 M Mg(AlCl$_2$EtBu)$_2$/THF electrolyte with Mg foil as counter electrode, the V$_2$O$_5$/GO composites could deliver a high capacity about 178 mAh g^{-1}, corresponding to 0.6 mol Mg^{2+} ions inserted into per formula unit of V$_2$O$_5$. After 20 cycles, the specific capacity of 140 mAh g^{-1} remains. This property is pretty well in the batteries that Mg metal is used as anodes directly. The disordered structure and superior recombination buffer the structure expansion/contraction and improve the electrolyte contact areas which shorten the Mg^{2+} ions transportation length. Furthermore, graphene also optimizes the electronic conductivity and stabilizes the structure in cycling performance. Although V$_2$O$_5$/GO could work in coin-type cells, the practical application of V$_2$O$_5$/GO in RMBs still needs further explorations.

Sulfur doping is an effective strategy to improve the capacity of materials [116]. From the researches about magnesium batteries, metal oxides materials often possess stable crystal structures and strong binding bonds that will result in the sluggish diffusion rate and large intercalation barrier of Mg^{2+} ions. On the other hand, Mg^{2+} ions also tend to be trapped in metal oxides materials more easily because of the large electronegativity of oxygen. So sulfur-doped methods and amorphous structures will bring more labile factors in materials and change the local charge distribution which will reduce the intercalation barrier of Mg^{2+} ions and improve the capacity of materials. Inamoto et al. [117] synthesized the sulfur-doped vanadium oxides (S-V$_2$O$_5$) with low-temperature plasma and a microwave generator. The surface of S-V$_2$O$_5$ might become amorphous and the electrochemical performance improved much. In S-V$_2$O$_5$, a capacity of 300 mAh g^{-1} was obtained while the pure orthorhombic V$_2$O$_5$ only exhibited a capacity of 170 mAh g^{-1}. Furthermore, different metal oxides, such as MnO$_2$, MoO$_3$, Fe$_2$O$_3$,

NiO, and ZrO$_2$, were composited with the S-V$_2$O$_5$ structure and their electrochemical performances improved in different degrees. From this work, sulfur doping and compositing with metal oxides are effective to improve the electrochemical performance of orthorhombic V$_2$O$_5$. However, sulfur doping might result in the low discharging voltage. To improve the discharging voltage in magnesiation process of V$_2$O$_5$, Arthur et al. [118] synthesized the amorphous V$_2$O$_5$–P$_2$O$_5$ via ball-milling and investigated the electrochemical performance of RMBs at different V$_2$O$_5$/P$_2$O$_5$ molar ratios. From the result, V$_2$O$_5$/P$_2$O$_5$ molar ratio of 3:1 achieved the high-voltage electrochemical magnesiation and the structures of compounds were investigated by XRD, NEXAFS, DSC, XPS. Large quantity of V^{4+} sites and PO$_4$ units result in the improved vitrification and the most atomic vacancies might be created at the terminally bonded or epaxial oxygen of V$_2$O$_5$. Compared with ordinary polycrystalline V$_2$O$_5$, the amorphous V$_2$O$_5$–P$_2$O$_5$ reached better electrochemical performance, owing to the increased interlayer spacing and the special V–O–P bond. Although recombination of P$_2$O$_5$ with V$_2$O$_5$ and amorphization method improved the discharging voltage, the reversibility of compounds and the non-corrosive, high-voltage electrolyte are still puzzles in this work.

Many researchers have demonstrated that pre-intercalating organics in V$_2$O$_5$ crystal structure could optimize the electrochemical performance [119–123]. Perera et al. [124] pre-intercalated different amounts of poly ethylene oxide (PEO) in the layers of V$_2$O$_5$ xerogels and controlled the interlayered spacing by using in situ sol–gel synthesis method. From high rate transmission electron microscopy (HRTEM), XRD, infrared (FTIR) and Raman spectroscopy results, the different quantities of PEO have been intercalated into V$_2$O$_5$ by in situ sol–gel synthesis method. With the increasing PEO content, the layers distance enlarged and the electrochemical property of Mg^{2+} ions storage improved in certain degree. V$_2$O$_5$-PEO could exhibit ~ 5 times of Mg^{2+} ions storage capacity and ~ 2 times higher diffusion coefficient compared with the ordinary V$_2$O$_5$. Moderate content of PEO will expand the interlayer spacing and shield the powerful polarization effect of divalent Mg^{2+} ions. But excessive PEO intercalation into the V$_2$O$_5$ will result in the deteriorated electrochemical performance, owing to lower diffusion of Mg^{2+} ions, lower electronic conductivity and the excessive coordination of PEO with V$_2$O$_5$ structure, which will block the Mg^{2+} ions diffusion. In this work, PEO is used as additive to expand the interlamellar spacing of V$_2$O$_5$ and shield the polarization effect of Mg^{2+} ions. Moreover, this work also makes it possible for aprotic constituents in organic electrolyte to co-intercalate in the cathode materials. Pre-intercalation is a meaningful method to activate the Mg^{2+} ions storage ability of materials. Pre-intercalated ions or compound will exploit the diffusion path and optimize the diffusion dynamics of transfer cations. Different

pre-intercalated materials or pre-intercalated extents will impact the electrochemical performance of cathode materials. For further development, the optimization mechanism of pre-intercalation needs to be explored more clearly.

Recently, Vadym et al. [125] concluded that VO_2 has the lower Mg^{2+} ions diffusion barrier of 0.33 eV compared with α-V_2O_5 (1.15 eV) and β-V_2O_5 (0.65 eV). Moreover, VO_2 has low-toxicity, structure diversity and more flexible structure compared with V_2O_5 [126, 127]. In this material, VO_6 octahedrons constitute the crystal structure in different connected ways and V–O tunnel could provide the diffusion path for Mg^{2+} ions. Luo et al. [127] reported the investigation of nanostructured $VO_2(B)$ as a high-voltage and high-capacity cathode material in RMBs. Nanostructured $VO_2(B)$ was measured in three-electrode system, in which carbon rod and Ag/AgCl electrode were used as counter and reference electrodes in 1 M $Mg(ClO_4)_2$/AN electrolyte. From the result, the electrochemical performance of $VO_2(B)$ nanorods is much better than that of VO_2 (B) nanosheets. In the first cycle, $VO_2(B)$ nanorods deliver a high capacity of 391 mAh g^{-1} at 25 mA g^{-1} while $VO_2(B)$ nanosheets deliver a capacity of 356 mAh g^{-1}. After 10 cycles, the capacity of $VO_2(B)$ nanorods remains at 94.7% but that of $VO_2(B)$ nanosheets only remains at 42%. The main reason for the better electrochemical performance of $VO_2(B)$ nanorods is that the special morphology obtains the faster ions diffusion rate and reduces the diffusion path [128]. Actual quantity of intercalated Mg^{2+} ions was detected by ICP, and the result was in accordance with the measured capacity. The authors also explored the structure changes of $VO_2(B)$ nanorods by the ex situ XRD analysis, from which amorphization trend was found in the cycling process, linking with the capacity fading. From XPS result, both V^{4+} (516.3 eV) and V^{5+} (519.0 eV) exist in the $VO_2(B)$ nanorods, and both of them are reduced to V^{3+} (515.1 eV) in discharge process. In this study, nanostructured $VO_2(B)$ is a promising high-capacity cathode material in RMBs but the detailed mechanisms remain to be further investigated. To assemble VO_2 with Mg anode directly and avert the incompatibility problem of $Mg(ClO_4)_2$/AN electrolyte with Mg anode, the magnesium storage performance of $VO_2(B)$ cathode material in $(PhMgCl)_2$–$AlCl_3$/THF electrolyte (APC) also has been reported [129]. However, the incompatibility problem between APC and vanadium oxides results in the poor electrochemical performance of $VO_2(B)$ in RMBs.

Except V_2O_5 and VO_2, many non-stoichiometric vanadium oxides have also attracted considerable interests as Mg^{2+} ions intercalation cathodes [130, 131]. Jiao et al. [130, 132] synthesized the open-ended $VO_{2.37}$ nanotubes through sol–gel reaction followed by hydrothermal treatment. These special nanotubes have the length of 1–3 μm and the outer diameter of 60–100 nm. Moreover, the inner diameter of

15–40 nm and the open tube ends structure are also found in the nanotube materials. In the 0.25 M $Mg(AlBu_2Cl_2)_2$/THF solution with Mg metal as counter and reference electrodes, $VO_{2.37}$ nanotubes exhibit a oxidation peak at 1.16 V and a redox peak at 0.92 V, which correspond to the (de)intercalation of Mg^{2+} ions. At 1 mA g^{-1}, $VO_{2.37}$ nanotubes deliver the discharge capacity of 76 mAh g^{-1} and Mg^{2+} ions diffuse much faster than that in polycrystalline V_2O_5 from the EIS results. From the XPS spectra and ex situ XRD patterns of the different-state $VO_{2.37}$ nanotubes, the *d* value of $VO_{2.37}$ gradually increases and V^{5+} is reduced to V^{4+} in the discharge process, and the Mg^{2+} ions will intercalate into the layer of the tubes. The open-ended $VO_{2.37}$ nanotubes with wide inner and outer diameters exhibit better electrochemical performance compared with the polycrystalline V_2O_5, which might result from the specific structure. First, in open-ended structure, Mg^{2+} ions could diffuse faster compared with the surface-to-bulk structure. Second, the diffusion path of cations is shorter than the ordinary structure. Finally, the open-ended tubes will provide large electrode–electrolyte contact areas in electrolyte-filled channels. Similar works were also reported by Ryoung-Hee et al. [131], and they synthesized the highly reduced VO_x nanotubes via microwave-assisted hydrothermal method with amine as reducing agent and organic template. VO_x mainly consists of distorted edge-shaped VO_5 pyramids with large-interlayer-distance layered structure [133]. Open-ended structure and rolled-tube shapes of VO_x nanotubes also exhibit in this work and the roll-tube comes from the octahedral VO_6 (V^{3+}) structure [131]. Two different kinds of VO_x (low and high concentrations of the amine template in VO_x are denoted as LT-VO_x and HT-VO_x) were measured in 0.5 M $Mg(ClO_4)_2$/AN electrolyte with magnesium alloy as counter electrode and Ag/$AgNO_3$ as reference electrode. Although LT-VO_x nanotubes exhibit higher specific capacity (230 mAh g^{-1}) than HT-VO_x nanotubes (218 mAh g^{-1}), the capacity retention of HT-VO_x nanotubes (70.8% after 20 cycles) is much higher than that of LT-VO_x nanotubes (24% after 20 cycles). In the EIS analysis, HT-VO_x nanotubes show lower charge transfer resistance than LT-VO_x nanotubes no matter in fresh state or after the first cycle. For explaining the excellent electrochemical performance of HT-VO_x nanotubes, the authors demonstrated that V^{3+} only exists in the HT-VO_x nanotubes, and thought that the existence of octahedral VO_6 (V^{3+}) in the HT-VO_x nanotubes enhances the mobility of Mg^{2+} ions in the crystal structure. Furthermore, VO_6 octahedron might expand the interstitial sites because of the higher coordination number and larger ionic size of V^{3+} ions compared with V^{4+} and V^{5+}. From this work, introducing the large V^{3+}-O cluster to activate the VO_4 tetrahedron and VO_5 square pyramid might be the feasible ways to improve the property of vanadium oxide materials in RMBs.

2.2 Vanadium Bronzes

Vanadium bronzes ($M_xV_yO_z$, M = metal elements), as a ternary compound, could have more stable structure owing to the M^{n+} ions that usually are sited between VO_x layers and act as "pillars". In 1995, Novak et al. reported about electrochemical insertion of Mg^{2+} ions into NaV_3O_8 and $Mg(V_3O_8)_2$ for the first time [103, 134]. In these kinds of vanadium bronzes, one vanadium atom is with a coordination number of 5, and the other two are with a coordination number of 6, accompanied by a distorted octahedron and elongated V–O bonds. $MgCl_2/AlCl_3/EMIC$ salt melt (liquid at room temperature) was chosen as electrolyte. For $Mg(V_3O_8)_2$, the high specific capacity about 150 mAh g^{-1} was obtained in the first cycle and more than 80 mAh g^{-1} could remain after 60 deep cycles. Unfortunately, the discharge capacity is always much higher than charge capacity in the first 15 cycles and the phenomenon that Mg^{2+} ions trapped in NaV_3O_8 bronze is severer than $Mg(V_3O_8)_2$. Partly irreversible Mg^{2+} ions might occupy some available insertion sites in the structure to smooth the diffusion path of Mg^{2+} ions, but the reason for the difference between NaV_3O_8 and $Mg(V_3O_8)_2$ is still unclear. On the other hand, the NaV_3O_8 ($Mg(V_3O_8)_2$) dried at different temperatures (50, 200 °C and higher temperature) have different electrochemical properties. The bronzes synthesized or dried at high temperature are less active than that in low temperature. From the FTIR, XRD and differential scanning calorimeter (DSC) results, slight variance in water content can be related to the different electrochemical property. The water molecules act as "spacers" and bonded water molecules also stabilize the lattice of bronzes when divalent Mg^{2+} ions diffuse in the structure. To take advantage of the shield effect of water molecules, $NaV_3O_8·1.69H_2O$ nanobelts were synthesized recently [135]. The novel room temperature synthetic method maintain the water in the structure. In addition, the $NaV_3O_8·1.69H_2O$ nanobelts exhibit high surface areas compared with commercial V_2O_5. In coin-type cell with APC electrolyte, $NaV_3O_8·1.69H_2O$ nanobelts exhibit high specific capacity of 110 mAh g^{-1} at 10 mA g^{-1}. At high current density, 80% capacity remains after 100 cycles. For increasing the specific capacity, the authors increased the cutoff voltage. However, with the increasing cutoff voltage, the coulombic efficiency will decrease due to the electrolyte decomposition. During cycling performance, no new phase is observed in the materials. But some Mg^{2+} ions will be trapped in the $NaV_3O_8·1.69H_2O$ nanobelts. Moreover, these trapped Mg^{2+} ions will affect the reversibility of battery and result in the low ions diffusion rate inside $NaV_3O_8·1.69H_2O$ nanobelts. In this work, the lateral confinement and high conduction channels of $NaV_3O_8·1.69H_2O$ nanobelts facilitate the electron movements along the nano-length axis. The fast insertion and extraction of Mg^{2+} ions are also attributed

to the shield effect of water. Reducing the internal resistance of trapped Mg^{2+} ions is the next problem to solve in the $NaV_3O_8·1.69H_2O$ nanobelts.

The bannermanite-type NaV_6O_{15} with monoclinic space group C2/m was also applied in RMBs recently [136]. In individual unit cell of NaV_6O_{15}, there is one oxygen atom linked with the V_6O_{15} layers and two interstitial cation-sites existing in tunnels that are connected with quasi-1D conductivity [137]. Although NaV_6O_{15} displays decent electrochemical property in dual-electrolyte solution ($Mg(BH_4)_2$ and $NaBH_4$ in DGM), it suffers poor electrochemical performance in RMBs (1 M anhydrous $Mg(ClO_4)_2$ in dry acetonitrile (AN) as electrolyte). In two-electrode configuration, NaV_6O_{15} suffers a rapid capacity decrease from 90 to 0 mAh g^{-1} in only 20 cycles and is accompanied by the increasing polarization and low efficiency. This phenomenon is caused by the passivation of negative electrode in the electrolyte. The poor electrochemical performance was ameliorated in the three-electrode configuration. In the first five cycles, the capacity increased from 90 to 210 mAh g^{-1} which probably resulted from the electrode activation. But the irreversible electrolyte decomposition and the formation of blocking layer on Mg surface caused the low coulombic efficiency in the next cycles [100]. In spite of the troublesome problem about electrolyte, NaV_6O_{15} is still a potential material in RMBs due to its high specific capacity and accessible synthesis methods.

2.3 Vanadium-Based NASICONs

Na super ionic conductors (NASICONs) have proven to be potential materials for lithium and sodium batteries because of high working voltage platform and excellent cations mobility in NASICONs [138–143]. $A_xM_2(PO_4)_3$ is the general chemical formula of NASICON in which A is metal cation such as Li^+, Na^+, K^+ and Mg^{2+} ion, M refers to transition metal such as Ti, Zr, V, Fe. Because of the high mobility of the monovalent cations in the structure, researchers also anticipate the good mobility of Mg^{2+} ions in NASICONs.

Huang et al. [144] firstly reported the vanadium-based phosphate ($Li_3V_2(PO_4)_3$) with electrochemical method to get monoclinic $V_2(PO_4)_3$-NASICON structure in RMBs. They first assembled the $Li_3V_2(PO_4)_3$ cathode with Mg rod and Ag/AgCl electrode as counter and reference electrodes in $Mg(TFSI)_2$/AN directly. Four little two-phase charge plateaus in 3.59, 3.68, 4.08 and 4.49 V were observed which linked with the three kinds of Li^+ ions extraction from the different crystallographic sites of intervals [145, 146]. During the discharge process, four voltage plateaus disappeared and gradual sloping single-phase discharge profile appeared. In this process, delithiated $V_2(PO_4)_3$ was generated from the cycling process and Mg^{2+} ions intercalation gradually substituted Li^+ ions intercalation process. To eliminate the impact of Li^+ ions

extracted from the $Li_3V_2(PO_4)_3$ in electrolyte, Huang et al. took the delithiated $V_2(PO_4)_3$ (charged state of $Li_3V_2(PO_4)_3$) into the new RMBs. After 5 cycles, the capacity of $V_2(PO_4)_3$ increased to 197 mAh g^{-1} (equal to the first discharge capacity of $Li_3V_2(PO_4)_3$). In this process, Mg^{2+} ions change from surface absorption and intercalation to "inner core" diffusion in the structure. Although the shift of the X-ray absorption spectroscopy (XAS) result testified the reduction of vanadium in the discharge process, the detailed reaction mechanism is still unclear. The discharge plateau at 1.5 V (vs. Mg/Mg^{2+}) still need to be understood more deeply [147–149]. Similar work about $Na_3V_2(PO_4)_3$ in hybrid batteries was also reported by Cabello et al. [150]. They found that 1.7 mol Na$^+$ will be extracted from the structure per formula unit in the first charge process. In this work, Mg metal is used as counter and reference electrode in Swagelok-type three-electrode cells and 0.5 M Mg(TFSI)$_2$/DME is used as electrolyte. Na$^+$ ions and Mg^{2+} ions will intercalate into $Na_{1.3}V_2(PO_4)_3$ at 1.6 and 1.2 V (vs. Mg/Mg^{2+}), respectively. This result is discrepant from the result of Li et al. [151]. Cabello et al. thought the differences of electrolyte and test methods resulted in the discrepancy. With the cycling process, Na$^+$ ions in electrolyte were consumed by deposit and Na$^+$ ions intercalation process became obscure. Thus, Mg^{2+} ions gradually dominated the intercalation process. The author also investigated the mechanism of Mg^{2+} ions electrochemical insertion process via assembling charged-state $Na_3V_2(PO_4)_3$ ($Na_{1.3}V_2(PO_4)_3$) in sodium-free electrolyte. During first discharge process, around 100 mAh g^{-1} capacity with discharge platform of 1.2 V (vs. Mg/Mg^{2+}) was obtained, which suggested the high feasibility of $Na_3V_2(PO_4)_3$ in RMBs. Zeng et al. [152] deeply investigated the Mg^{2+} ions storage property of high-voltage mesoporous $Na_3V_2(PO_4)_3$/C in sodium-free electrolyte. To avert the passive problem on Mg surface in conventional electrolytes, they chose active carbon and Ag/AgCl as counter and reference electrodes in Mg(TFSI)$_2$/AN electrolyte which would be more compatible with high-voltage mesoporous $Na_3V_2(PO_4)_3$/C. At 20 mA g^{-1}, desodiated $NaV_2(PO_4)_3$ (ED-NVP) obtained a high discharge platform at 2.58 V (vs. Mg/Mg^{2+}) and delivered the capacity of 88.8 mAh g^{-1} with high coulombic efficiency (Fig. 2g). After 100 cycles, 81% specific capacity remained (Fig. 2h). Compared to other NASICONs in RMBs, this mesoporous $Na_3V_2(PO_4)_3$/C exhibited a higher discharge voltage platform and more stable cycling performance [144, 150]. Specific spray drying-annealing synthetic method and carbon-coated strategy modified the electrochemical performance of NASICON in Mg^{2+} ions diffusion, which enlightened further work about NASICONs. The electrochemical reaction mechanism of $Na_3V_2(PO_4)_3$/C was investigated by ex situ XRD, XPS and galvanostatic intermittent titration technique (GITT) measurements. When Na$^+$ ions deintercalated from the $Na_3V_2(PO_4)_3$, the volume of unit cell decreased. After Mg^{2+} ions inserted to ED-NVP, the lattice constant enlarged, accompanied by

the shrinkage of V–O bonds. But the lattice volume of magnesiated phase is still smaller than that of $Na_3V_2(PO_4)_3$. The smaller size of Mg^{2+} ions (0.72 ppm) than Na$^+$ ions (1.02 ppm) might result in this phenomenon. Moreover, some Na$^+$ ions in 6b sites of ED-NVP might also be extracted from the structure partly, resulting in the volume decrease of structure. The XPS analysis illustrated that magnesiation process was accompanied by the redox of V^{4+} to V^{3+}. From the GITT curves, the minimum apparent diffusion coefficient in discharge and charge platform accounted for the two-phase transition process in materials. This similar phenomenon is also observed in LiFePO$_4$, $Li_3V_2(PO_4)_3$ and other phosphate-based materials in Li-ion batteries [153–155].

2.4 Other Vanadium-Based Materials

Kaveevivitchai et al. [156] synthesized the unique $Mo_{2.48}VO_{9.93}$ material with three-dimensional microporous framework structure and examined Mg intercalation performance. The pentagonal $[(Mo)Mo_5O_{27}]$ units and corner-sharing MO$_6$ (M = Mo or V cations) octahedra constitute the layered structure of the $Mo_{2.48}VO_{9.93}$, which stacks along c axis and forms a microporous framework with three, six and seven ring tunnels (Fig. 3a). The large open ring tunnel preferentially provides active sites for the diffusion of Mg^{2+} ions and buffers the structure volume change when strongly polarized Mg^{2+} cations diffuse in channel. When $Mo_{2.48}VO_{9.93}$ was assembled with active carbon as counter and reference electrodes in 0.5 M Mg(TFSI)$_2$/AN electrolyte, high capacity of 379 mAh g^{-1} (corresponding to 3.49 mol Mg^{2+} ions inserted into $Mo_{2.48}VO_{9.93}$ per formula unit) was obtained at low rate of C/70 (2 mA g^{-1}). But after 10 cycles, only 62% capacity (235 mAh g^{-1}) remained (Fig. 3b). On the contrary, at higher rate of C/70 (4 mA g^{-1}), $Mo_{2.48}VO_{9.93}$ could cycle with no capacity faded during the first 25 cycles. When inserted number of Mg^{2+} ions are small ($Mg_xMo_{2.48}VO_{9.93}$, $0 \leq x \leq 1$), Mg^{2+} ions were preferentially inserted into the six- and seven-membered ring channels. The large channels (3 Å for six- and 5 Å for seven-membered ring channels) allowed the rapid diffusion of guest cations and could shield or sustain the structure change. But when $1 \leq x \leq 3.49$, too many Mg^{2+} ions were inserted into the structure and they were forced to diffuse in the three-membered ring channels which might result the contact problem of ring channels, structure destruction and irreversible intercalation of Mg^{2+} ions. For examining the structure change of materials in charge and discharge process, the author simulated the electrochemical insertion process of Mg^{2+} ions based on chemical redox intercalation of $Mo_{2.48}VO_{9.93}$ ($Mg_xMo_{2.48}VO_{9.93}$, $0 < x \leq 3.49$). Considering the Le Bail refinement (Fig. 3c, d) and changes of the lattice parameters of $Mg_xMo_{2.48}VO_{9.93}$, when $x < 1$, a and b parameters of $Mg_xMo_{2.48}VO_{9.93}$ change slowly. But when

$x > 1$, a and b parameters will increase significantly and c parameter remains constant, which explains the drastic extension in a–b dimension layers when too many Mg^{2+} ions intercalate into materials. This novel work provides many realistic strategies for Mg^{2+} ions storage. First, synthesizing the materials with microporous framework structure which could provide the large size migration channels and activate more vacant sites for transporting Mg^{2+} ions is an efficient method. On the other hand, adjusting the number of intercalated cations could maintain the structure stability in cycling performance. Recently, Miao et al. [157] reported the electrospun V_2MoO_8 as cathode materials for RMBs. This work researched the materials electrochemical properties in APC partly. Although the initial discharge capacity of V_2MoO_8 is 200 mAh g^{-1} with the plateau of 0.96 V, the capacity is just 30% of that in the second cycle and discharge plateau disappears. This phenomenon exists in many oxide materials when nonaqueous organic solvents are applied, in which solvation process of Mg^{2+} ions in electrolyte might affect the de-intercalation process [158–160].

Minella et al. [161] first reported the VOCl as cathode materials for RMBs and adopted the strategy to open the interlayer spacing via preliminary cycling in Li-ion battery. This orthorhombic VOCl has the sandwiched structure that chlorine layers stack on the buckled V–O bilayers. VOCl could deliver a high capacity of 260 mAh g^{-1} if 0.5 M Mg^{2+} ions intercalated in the sandwiched structure. But in (HMDS)$_2$Mg/DEG/TEG electrolyte (hexamethyldisilazide = HMDS, diglyme = DEG, tetraglyme = TEG, DEG:TEG = 1:1 in volume), only a low capacity of 45 mAh g^{-1} was obtained at 10 mA g^{-1} in the first cycle and only 70% capacity remained after 20 cycles. The author did not explain the gap between measured capacity and theoretical capacity but hypothesized that preliminary insertion of Li^+ ions would expand the interlayer distance of VOCl in (001) direction and facilitate the intercalation process of Mg^{2+} ions. After 20 cycles in Li/LiPF$_6$-EC:DMC/VOCl, the Li-cycled-VOCl electrode could obtain a capacity of 185 mAh g^{-1} and a relative high capacity of 107 mAh g^{-1} remained after 40 cycles in RMBs. From HRTEM micrographs, the van der Waals bonded layer (001)$_{VOCl}$ expanded about 0.63 nm (from 0.79 to 1.42 nm) after cycling process in lithium battery. The more distorted and enlarged crystal lattice might explain the promotion of electrochemical property in Mg^{2+} ions storage. This work adopted a quick in situ method to modify the layered nanostructures and provided an exercisable stratagem to relieve the problem about compatibility between nonaqueous electrolyte and vanadium oxide.

First-principle calculation predicts that Mg^{2+} ions could diffuse in the calcium ferrite (CF) structure, which belongs to the post-spinel structure family. Especially, Mg^{2+} ions migration barriers will be below 400 meV in the desodiated-CF $NaV_{1.25}Ti_{0.75}O_4$ materials from calculated results

[162–164]. Recently, Sun et al. [164] examined the electrochemical performance of CF-type-tunnel-structured $NaV_{1.25}Ti_{0.75}O_4$ in RMBs. Firstly, Na^+ ions were extracted by chemical oxidation or electrochemical method. In different chemical oxidation process, two kinds of desodiated $NaV_{1.25}Ti_{0.75}O_4$ ($Na_{0.25}V_{1.25}Ti_{0.75}O_4$ and $Na_{0.36}V_{1.25}Ti_{0.75}O_4$) can be obtained. In deep desodiation process, amorphization and structure collapses might occur, which will impact the performance of RMBs. In electrochemical desodiation process, the final composition is $Na_{0.44}V_{1.25}Ti_{0.75}O_4$, possessing higher Na content compared with that from chemical oxidation. Then, the authors assembled these desodiated materials with Mg metal anode in monocarborane electrolyte (($Mg(CB_{11}H_{12})_2$ in tetraglyme). In the first cycle, $Na_{0.25}V_{1.25}Ti_{0.75}O_4$ could obtain the capacity of 80 mAh g^{-1} at the current density of 5 mA g^{-1} while $Na_{0.44}V_{1.25}Ti_{0.75}O_4$ only exhibited 60 mAh g^{-1}. The greater Na^+ ions content might affect Mg^{2+} ions migration pathways. However, due to the electrochemically inactive amorphous phase and the structure degradation, both $Na_{0.25}V_{1.25}Ti_{0.75}O_4$ and $Na_{0.44}V_{1.25}Ti_{0.75}O_4$ suffered from the severe capacity decay in the second cycle. In this work, although the desodiated $NaV_{1.25}Ti_{0.75}O_4$ exhibits the poor electrochemical performance, the metastable phases could provide a lower energy barrier for Mg^{2+} ions diffusion, which is significant to the further research.

3 Vanadium-Based Compounds for Rechargeable Zinc Battery System

RZBs not only possess high energy density but also have high power density, which is important in practical application. Zn metal has attracted much attention in these years for environmentally friendly, low cost, high security, high conductivity and abundant reserves. More importantly, Zn metal could dissolve and deposit steadily in aqueous electrolyte, making it possible to assemble high-performance aqueous RZBs. There are plenty of vanadium-based materials that are compatible in aqueous electrolyte and possess electrochemical activity for Zn^{2+} ions storage. The earliest studies were mostly focused on vanadium oxides, such as V_2O_5. Afterward, vanadate compounds became the hot zone, due to the stable structure caused by the interlayer cations. Meanwhile, some other types of vanadium-based materials have also been reported, like NASICONs, which show a different zinc storage mechanism. Details of these works will be discussed below.

3.1 Vanadium Pentoxide

Bilayer V_2O_5 with large interlayer spacing is a promising material for Zn^{2+} ions intercalation/de-intercalation.
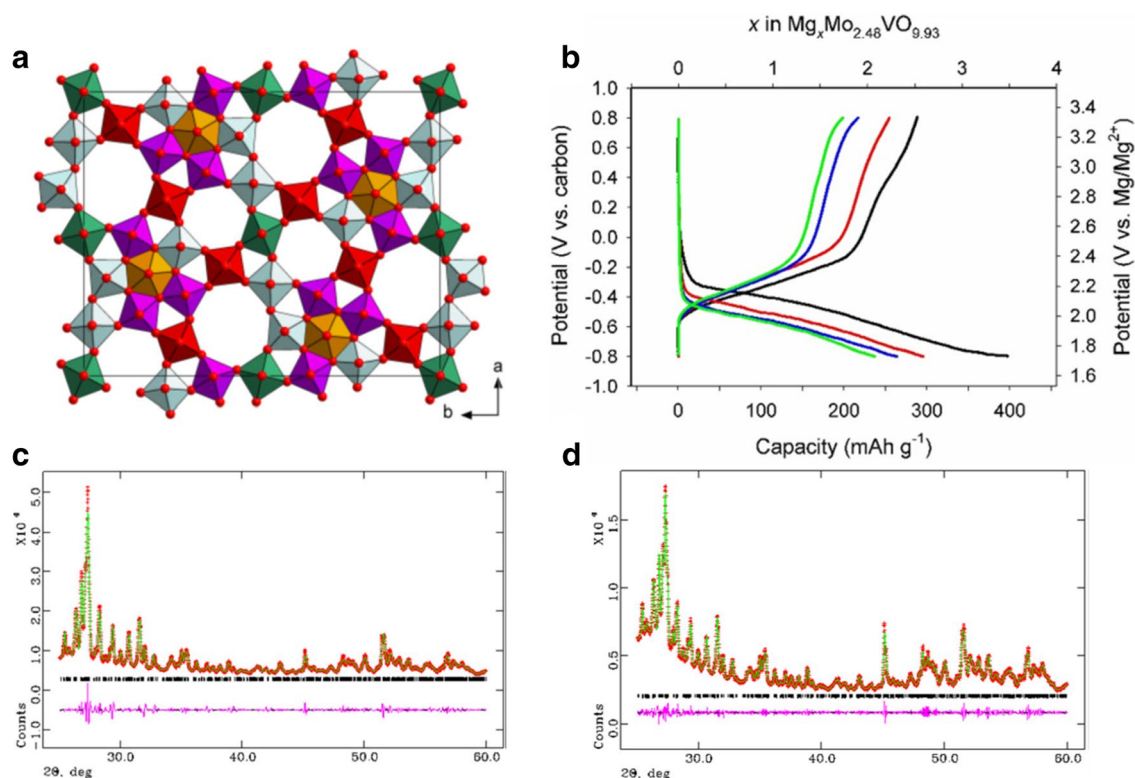
Fig. 3 a Structure of $Mo_{2.48}VO_{9.93}$ viewed down the *c* axis (green, Mo^{5+}/V^{4+}; red, Mo^{6+}/V^{5+}; blue, Mo^{6+}/Mo^{5+}; orange, Mo^{5+}; and purple, Mo^{6+}), **b** electrochemical discharge–charge profiles of AC/$Mo_{2.48}VO_{9.93}$ cell at 2 mA g^{-1}: 1st cycle, black; 2nd cycle, red; 5th cycle, blue; 10th cycle, green. Le Bail refinements of **c** $Mo_{2.48}VO_{9.93}$ and **d** $Mg_{1.5}Mo_{2.48}VO_{9.93}$. Figure **a–d** reproduced with permission [156]. Copyright 2016, American Chemical Society

Recently, Yan et al. [165] explored $V_2O_5 \cdot nH_2O$/graphene (VOG) as cathode material for RZBs. The reduced graphene oxide supported $V_2O_5 \cdot nH_2O$ nanowire framework could significantly increase the conductivity of cathode and enhance contact between electrolyte and active material, resulting in higher ion diffusion coefficient. This aqueous Zn/V_2O_5 system displays a capacity of 295 mAh g^{-1} at a power density of 6.4 kW kg^{-1}, and an initial capacity of 381 mAh g^{-1} is obtained (Fig. 4a). The cycling performance at 6 A g^{-1} was also investigated, which showed that 71% of maximum capacity could be achieved after 900 cycles (Fig. 4b). For the control experiment, VOG-350 (prepared by annealing $V_2O_5 \cdot H_2O$/graphene at 350 °C for 2 h in vacuum to eliminate structural water) displayed a poorer cycling performance than that of VOG. This result reveals the positive impact of structural H_2O on Zn^{2+} ions intercalating into bilayer $V_2O_5 \cdot nH_2O$. They further demonstrated it with XRD study and NMR (nuclear magnetic resonance) analysis, proposed that the effective charge of Zn^{2+} could be reduced by water solvation, leading to reduction of electrostatic interactions between Zn^{2+} ions and V_2O_5 framework, which can effectively promote its diffusion. The crystal structures of VOG at different states (pristine, charge to 1.3 V and discharge to

0.2 V) are shown in Fig. 4c. The crystal structure of VOG is fully reversible during charging and discharging process, when Zn^{2+} ions are extracted from the interlayer in charging process, the interlayer spacing will contract from 12.6 to 10 Å. In discharging process, there are two stages in Zn^{2+} ions intercalation. First, 0.3 mol Zn^{2+} ions will intercalate into the interlayer spacing and the voltage will decrease from 1.1 to 0.8 V. There is no phase transformation in this process. In the second discharge process of 0.6–0.4 V, a new phase with larger interlayer distance of 13.5 Å is generated, which links with the intercalation of Zn^{2+} ions. This phenomenon is different from the reaction process of $Zn_{0.25}V_2O_5$, where the interlayer distance will decrease with Zn^{2+} ions intercalation [165]. In VOG, coexistence of structural water enlarges the distance between neighboring oxygen ions and Zn^{2+} ions. Moreover, the water-based shielding layer relieves the polarization of Zn^{2+} ions and reduces electrostatic bond strength. These processes result in the lattice expansion when Zn^{2+} ions intercalate into the VOG and provide the higher diffusion coefficient of Zn^{2+} ions.

Besides aqueous RZBs system, the hydrated V_2O_5 has also been studied in nonaqueous RZBs system. Senguttuvan et al. [166] assembled a Zn/V_2O_5

system which utilized nonaqueous acetonitrile-zinc(II) bis(trifluoromethanesulfonyl) imide ((AN)-Zn(TFSI)$_2$) electrolyte. They introduced carbon foam as substrate on which the V$_2$O$_5$ could grow via electrodeposition technique. The carbon foam not only serves as substrate but also accelerates the transmission of electrons. The reaction schematic and the electrochemical performances of V$_2$O$_5$/CFS are shown in Fig. 4d–f, the capacity and the long cycling performance are no match for the above-mentioned aqueous systems, but its coulombic efficiencies are close to 100% and higher than those of the aqueous systems. In aqueous RZBs system, it is usually not the pure Zn^{2+} ions that are inserted/extracted into/from the host materials. In fact, the Zn^{2+} ions involved in reaction are hydrated. However, the exact amount of water molecules in the first hydration layer is still uncertain. Most researchers believe that the hydrated Zn^{2+} ions are preferable to (de)intercalate from/into host materials, owing to the reduced electrostatic interactions. This may be the reason why the electrochemical performance of aqueous system is superior to nonaqueous system. Compared with aqueous RZBs, the nonaqueous RZBs are not restricted by decomposition voltage of water. Thus, achieving high voltage and high power density could be a practicable goal for nonaqueous RZBs.

In 2016, Linda and co-workers reported a layered Zn$_{0.25}$V$_2$O$_5$·nH$_2$O nanobelt utilized as cathode materials in aqueous RZBs [167]. This Zn$_{0.25}$V$_2$O$_5$·nH$_2$O nanobelt is synthesized by a microwave hydrothermal method. Compared with traditional hydrothermal method, the microwave-assistant method could dramatically reduce the time of heating process, increase product yield, and enhance product purity [168]. The structure of Zn$_{0.25}$V$_2$O$_5$·nH$_2$O consists of V$_2$O$_5$ framework with two-dimensional double-sheet structure (Fig. 5a), which is similar to the δ-V$_2$O$_5$ layers. This V$_2$O$_5$ framework extends infinitely in the *a–b* plane. The ZnO$_6$ octahedra, sited at the interspace between V$_2$O$_5$ layers, act as pillars. These pillars pin the V$_2$O$_5$ layers into a framework and stabilize the paths that accommodate intercalation of additional Zn^{2+} ions on discharge. The Zn/Zn$_{0.25}$V$_2$O$_5$ cell exhibits high capacity (250–300 mAh g^{-1}) and long cycling life in the 0.5–1.4 V (vs. Zn/Zn^{2+}) (Fig. 5b). The high capacity of 200 mAh g^{-1} is obtained after 1000 cycles at 2400 mA g^{-1}. During the insertion/extraction of Zn^{2+} ions, the structural water and indigenous Zn^{2+} ions act as pillars, contributing to stabilization of the layered structure and mobilizing cation migration. There is also a reversible water intercalation into Zn$_{0.25}$V$_2$O$_5$·nH$_2$O when the electrode is immersed in electrolyte, and the water de-intercalation is accompanied by Zn^{2+} intercalation upon electrochemical discharge. The mechanism is shown in Fig. 5a, c. Reaction can be written as the following equation (without regard to the additional water from the electrolyte):

$$Zn_{0.25}V_2O_5 \cdot nH_2O + 1.1Zn^{2+} + 2.2e^- \longleftrightarrow Zn_{1.35}V_2O_5 \cdot nH_2O.$$
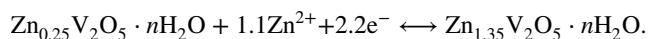
Notably, the influences of structural water on electrochemical performance have been discussed in Zn$_{0.25}$V$_2$O$_5$·nH$_2$O and V$_2$O$_5$·nH$_2$O. It is well established that the structural water is beneficial to aqueous battery system, owing to its "lubricating" effect and stabilization of structure. These works reveal a road for cathode materials design. At least, it is worth exploring more hydrated materials in research field of aqueous RZBs.

In addition to pre-intercalation of Zn in V$_2$O$_5$, there are also researches that pre-intercalated other elements into V$_2$O$_5$. He et al. [169] recently reported a Na$_{0.33}$V$_2$O$_5$ cathode material for RZBs. The Na$_{0.33}$V$_2$O$_5$ nanowire has a length of a few micrometers and a diameter of about 50–200 nm. In this Na$_{0.33}$V$_2$O$_5$, the vanadium has three sites. The V(1) and V(2) form V(1)O$_6$ and V(2)O$_6$ octahedrons with O atoms, respectively, and then constitute the [V$_4$O$_{12}$]$_n$ layers. The V(3) and O atoms form V(3)O$_5$ polyhedrons which joint the 2D [V$_4$O$_{12}$]$_n$ layers and lead to a 3D structure. The pre-intercalated Na$^+$ ions occupy the gaps between [V$_4$O$_{12}$]$_n$ layers and act as pillars, which could stabilize the structure of material. This structure results to an excellent long cycling performance. The Na$_{0.33}$V$_2$O$_5$/Zn system displays a capacity retention of ~93% after 1000 cycles at 1.0 A g^{-1}. Besides the stabilization of structure, the pre-embedded Na$^+$ ions could also greatly improve the conductivity. They demonstrated it by EIS measurements, the R_{ct} of Na$_{0.33}$V$_2$O$_5$ during the first cycle is 5.6 Ω, which is 2/3 of R_{ct} in V$_2$O$_5$. The EIS results are influenced by conductive additives and binders in electrode. To avoid this influence, they directly test the conductivity of single nanowire. Comparing with the conductivity of V$_2$O$_5$ (7.3 S m^{-1}), the conductivity of Na$_{0.33}$V$_2$O$_5$ (5.9×10^4 S m^{-1}) is increased by three orders of magnitudes. The authors also investigated the phase change of materials in cycling. When discharge process was from 1.6 to 0.7 V, only the change of interlayer distance was observed. During the deeper discharge process from 0.7 to 0.2 V, new phase (Zn$_x$Na$_{0.33}$V$_2$O$_5$, 0.42 < x < 0.96) emerged. The transition from Na$_{0.33}$V$_2$O$_5$ to Zn$_x$Na$_{0.33}$V$_2$O$_5$ was incomplete, there was still slight Na$_{0.33}$V$_2$O$_5$ that remained after the material discharged to 0.2 V. Through the whole discharge and charge process, the Na$^+$ ions are steady between the [V$_4$O$_{12}$]$_n$ layers, which proves the superior stability of Na$_{0.33}$V$_2$O$_5$.

3.2 Vanadate

Xia et al. [170] adjusted the reaction parameters of the above Zn$_{0.25}$V$_2$O$_5$·nH$_2$O nanobelts and successfully obtained Zn$_3$V$_2$O$_7$(OH)$_2$·2H$_2$O. This material structure is constructed by brucite type zinc oxide layers (differs from the double-sheet type 2D V$_2$O$_5$ framework of Zn$_{0.25}$V$_2$O$_5$·nH$_2$O) separated by V$_2$O$_7$ polyhedra. In the close-packed layers of O atoms, three of four octahedral sites are occupied by Zn atoms. The large cavities between layers are filled by water molecules randomly.
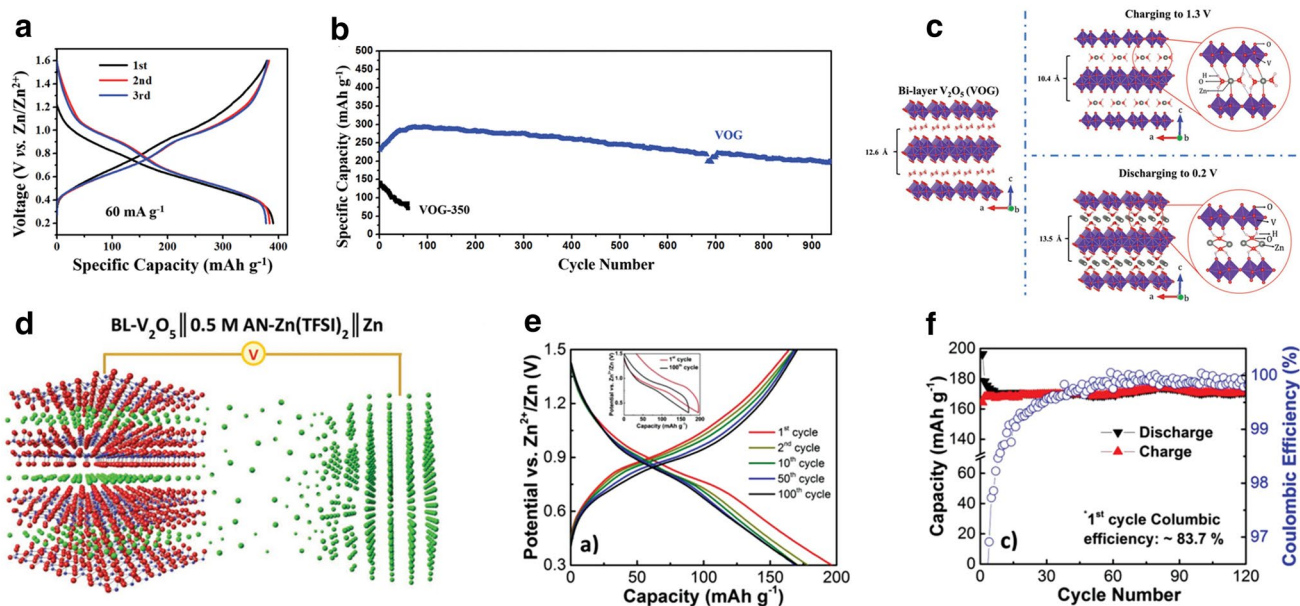
Fig. 4 a Charge–discharge curves for the first three cycles of the as-prepared VOG. b cycling performance of VOG and VOG-350 at 6 A g⁻¹. c The proposed crystal structures of pristine VOG, VOG after charging to 1.3 V, and discharging to 0.2 V. Figure a–c reproduced with permission [165]. Copyright 2017, Wiley–VCH. d schematic diagram of a Zn/V$_2$O$_5$ cell (red: oxygen, green: zinc, blue: vanadium), e charge–discharge curves and f cycling performance of V$_2$O$_5$/CFS cell at 14.4 m A h g⁻¹. Figure d–f reproduced with permission [166]. Copyright 2016, Wiley–VCH

The Zn$_3$V$_2$O$_7$(OH)$_2$·2H$_2$O cathode delivers capacities of 213 and 76 mAh g⁻¹ at current densities of 50 and 3000 mA g⁻¹, respectively. A reversible capacity of 101 mAh g⁻¹ could be obtained after 300 cycles, with a capacity retention of 68%. In particular, the estimated energy density of this cell is about 214 Wh kg⁻¹, which is relatively high compared with other vanadium-based materials or even with commercial lead–acid batteries. The electrochemical reaction in cathode can be described by the following equations:

$$Zn_3V_2O_7(OH)_2 \cdot 2H_2O + 1.9Zn^{2+} + 3.8e^-$$
$$\longleftrightarrow Zn_{4.9}V_2O_7(OH)_2 \cdot 2H_2O .$$
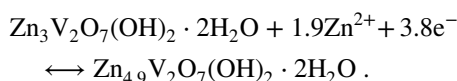
There is no obvious phase change during the Zn^{2+} ions insertion into Zn$_3$V$_2$O$_7$(OH)$_2$·2H$_2$O, but for LiV$_3$O$_8$, the reaction process is different. The electrochemical performance of LiV$_3$O$_8$ as cathode material for RZBs was reported by Alfaruq et al. [171], and its phase transition during (de) intercalation of Zn^{2+} ions was also deeply investigated. It delivers an initial capacity of over 250 mAh g⁻¹ at a current density of 16 mA g⁻¹ (Fig. 6a, b). There is an obvious difference between the charge curves and discharge curves that the charge curves have only one plateau while the discharge curves have two. This difference is caused by the different mechanisms between charge and discharge processes (Fig. 6c). In in situ XRD patterns, the (100) peak has significant changes in discharging process (Fig. 6d). In the period of 1.28–0.82 V, the peaks only change their positions,

corresponding to a solid-solution behavior of single-phase domain, and a ZnLiV$_3$O$_8$ mesophase is firstly formed at the same time. In the period of 0.81–0.7 V, the peak shifts are accompanied by splitting of (100) peak, corresponding to two-phase reactions and the formation of Zn$_y$LiV$_3$O$_8$ phase ($y > 1$). Four new peaks emerging in XRD pattern also demonstrate the formation of new phase. After the material discharges to 0.6 V, the peak shifts to higher degree, which reflects the shrinkage of interlayer spacing. This anomalistic shrinkage has also been reported in some other works based on the layered vanadate structure [172]. A mainstream explanation is that the shrinkage is caused by the electrostatic interaction between inserted cations and layers. By contrast, during charging process, the Zn$_y$LiV$_3$O$_8$ directly transforms to LiV$_3$O$_8$, which coincides with the typical single-phase behavior.

Among all the vanadium-based cathode materials for RZBs, the H$_2$V$_3$O$_8$ nanowires cathode reported by He et al. [173] owns the relatively high capacity. It delivers a high initial capacity of 423.8 mAh g⁻¹ at 100 mA g⁻¹, and also shows excellent cycling stability with a capacity retention of 94.3% over 1000 cycles at 5 A g⁻¹ (Fig. 6e). Such an excellent cycling performance not only profits from the intrinsic structure of this material, but also relates to the Zn(CF$_3$SO$_3$)$_2$ electrolyte they used. The bulky CF$_3$SO$_3^-$ anions in Zn(CF$_3$SO$_3$)$_2$ electrolyte can decrease the number of water surrounding Zn^{2+} ions, reduce solvation effect, resulting in
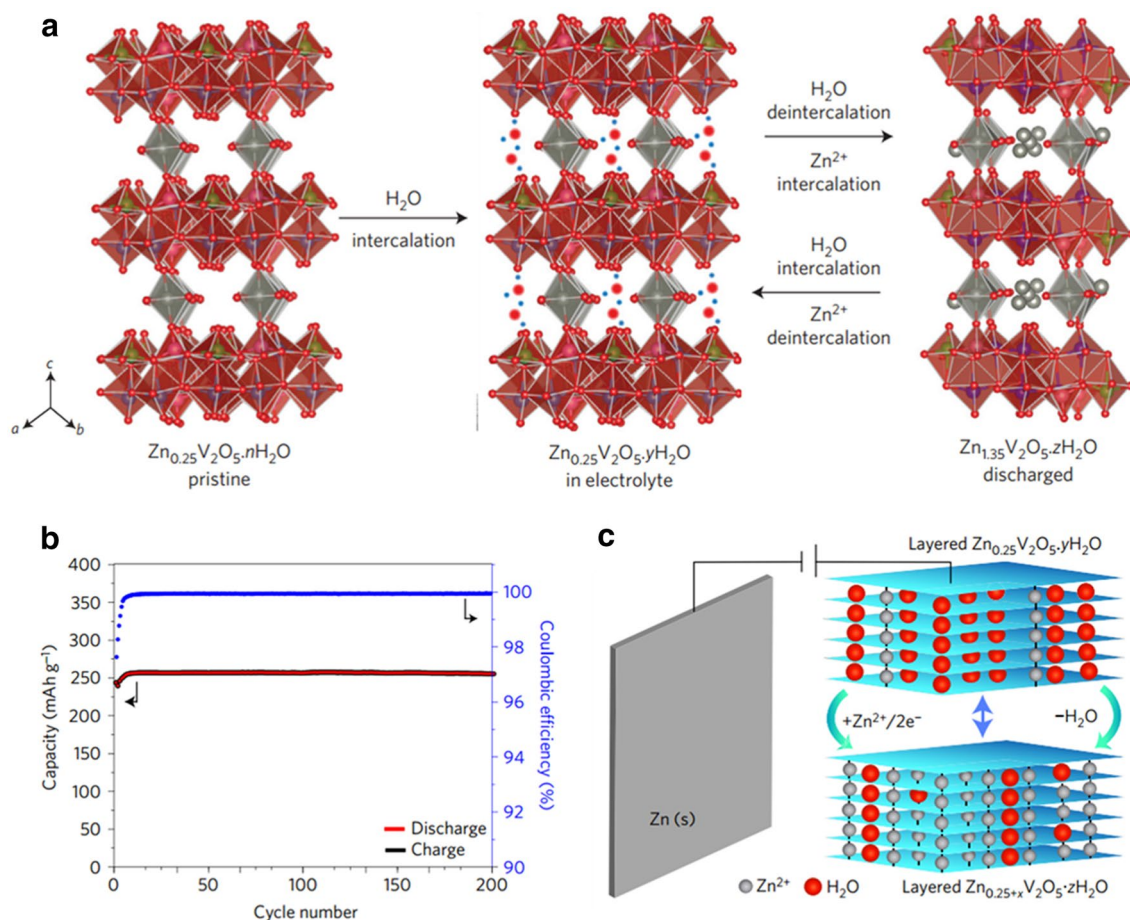
a better electrochemical performance than aqueous $ZnSO_4$ electrolyte. On the other hand, each V_3O_8 layer of $H_2V_3O_8$ consists of VO_6 octahedra and VO_5 trigonal bipyramids, forming platforms that are parallel to (001) lattice. These layers are connected by weak hydrogen bonds, which are believed beneficial to reversible (de)intercalation of ions. It is worth mentioning that during the long cycling process, an initial discharge capacity of 173.6 mAh g^{-1} is obtained, but it immediately drops to 130.6 mAh g^{-1} after 20 cycles. Then the capacity rises to approximately 140 mAh g^{-1}. The fading of capacity in the initial 20 cycles might be caused by the fact that at such a high rate, the electrolyte could gradually penetrate into interlayer space of active material in cathode. Then the electrolyte facilitates the electrochemical reaction, resulting in the increase in capacity, which tends to be stable at last. This kind of fade-recover phenomenon has been reported in some other works that utilize layered structure compounds as cathode materials based on intercalation mechanism [174–176].

3.3 Vanadium-Based NASICONs

There are plenty of vacancies in NASICONs structure that can store metal ions. The radius of Zn^{2+} ion is 0.74 Å, smaller than that of Na^+ ion, indicating a possibility for Zn^{2+} ions to be stored in these kind of materials.

Li et al. [177] synthesized the $Na_3V_2(PO_4)_3$ and applied it in RZBs. To offset the poor conductivity, they wrapped the $Na_3V_2(PO_4)_3$ nanoparticles with graphene-like carbon. The as-synthesized sample delivered a capacity of 97 mAh g^{-1} at 50 mA g^{-1} (Fig. 7a) and capacity retention of 74% after 100 cycles (Fig. 7b). Specially, the $Na_3V_2(PO_4)_3$/Zn system owns the highest voltage platforms (about 1.1 V while it discharges) among all these vanadium-based compounds. The reaction mechanism of $Na_3V_2(PO_4)_3$ is also based on (de)intercalation process, but is slightly different from the other materials discussed above. During the first charge process, 2/3 of Na^+ ions in $Na_3V_2(PO_4)_3$ are extracted from cathode. During the following cycles, the Zn^{2+} ions are intercalated/extracted

in/from the $NaV_2(PO_4)_3$, and no Na^+ ions are evolved. (Fig. 7c) From the Rietveld-refined XRD patterns, shrunk lattice constant can be found and this phenomenon might result from the higher charge density of intercalated Zn^{2+} ions or new vacancies in the crystal structure. On the other hand, Zn^{2+} ions might occupy both 18e and 6b sites and change the occupation sites during the insertion process. From the ex situ XPS results, when Na^+ ions are extracted from the crystal structure in the first charging process, V^{3+} will be oxidized to V^{4+}. After discharge process, V^{4+} is reduced back to V^{3+} and some Zn^{2+} ions might intercalate into the structure irreversibly. They also introduced cyclic voltammogram analysis to investigate the reaction kinetics. The b-values ($i = av^b$) calculated from measured results are close to 0.5 at all scan rates, shows a diffusion-dominated process through reaction ($b = 1$ means a capacitive behavior, while $b = 0.5$ corresponds to a strictly diffusion limited reaction) [178]. Though the electrochemical performance in this work might seem not dramatic, this work provides a new idea to fabricate RZBs with NASICONs.

$Na_2VTi(PO_4)_3$ is a related compound with $Na_3V_2(PO_4)_3$ obtained by substitution of half of the vanadium with titanium. According to the work of Mason and Lange [179], the $Na_2VTi(PO_4)_3$ also shows ability to store Zn^{2+} ions. The electrode was first cycled in Na_2SO_4 electrolyte to extract

Na^+ ions [similar to $Na_3V_2(PO_4)_3$ mentioned above], then washed and placed into $ZnSO_4$ electrolyte. Compared with vanadium ion, Ti^{4+} is more stable in aqueous solution, because it could form oxides with different levels of hydration. A passivation would occur when it is attacked by components of aqueous electrolyte. However, the capacity are mostly contributed by vanadium, so this replacement might cause the reduction of capacity. There are other ways to stabilize electrode in aqueous electrolyte, for instance, Pan et al. inhibited the disproportionation of Mn^{2+} in aqueous α-MnO_2/Zn system by introducing $MnSO_4$ as additive in $ZnSO_4$ electrolyte [50]. The $MnSO_4$ additive can change the equilibrium of Mn in electrolyte and thus suppresses the dissolution of Mn from MnO_2 in cathode. This work could inspire a new method to relieve the dissolution problem in some vanadium-based materials. The replacement of V in $Na_3V_2(PO_4)_3$ causes the reduction of capacity, but adjustment on electrolyte might also stabilize the aqueous system without such a capacity fading.

3.4 Other Vanadium-Based Materials

VS_2 as a typical member of transition metal dichalcogenides (TMDs) has hexagonal structure with interlayer spacing of 5.76 Å. Because of the direct bandgap, fast ion diffusion
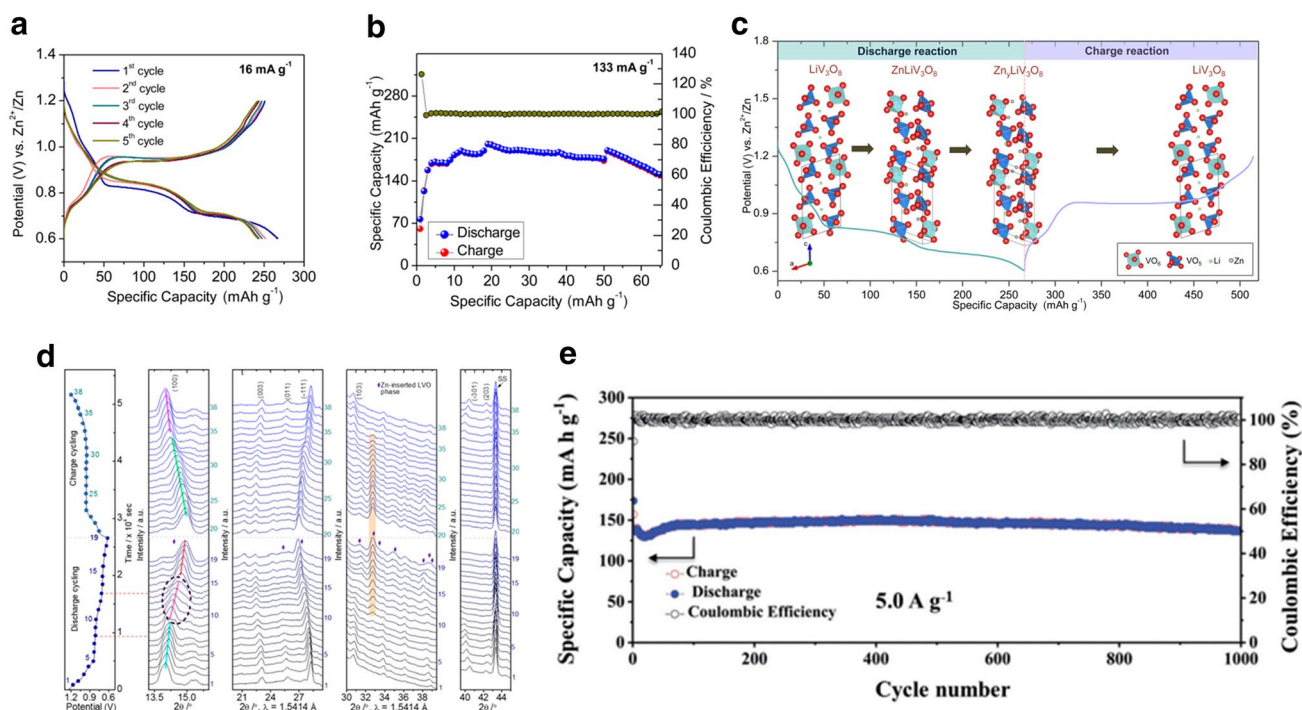

Fig. 6 **a** Initial five voltage profiles of the LiV_3O_8 electrode at a current density of 16 mA g^{-1}, **b** cycling performance and corresponding coulombic efficiencies of LiV_3O_8 between 0.6 and 1.2 V versus Zn/Zn^{2+} at 133 mA g^{-1}, **c** schematic of the Zn-intercalation mechanism in the present LiV_3O_8 cathode, **d** in situ XRD patterns obtained within selected scanning angle (2θ) domains. Figure **a**–**d** reproduced with permission [171]. Copyright 2017, American Chemical Society, **e** prolonged cycling performance of $H_2V_3O_8$ at high rate (5.0 A g^{-1}), reproduced with permission [173]. Copyright 2017, Wiley–VCH

and graphene-like layered structure, VS_2 has attracted much attention as energy storage materials. VS_2 possesses the sandwiched structure which consists of one vanadium layer and two sulfur layers. In the sandwiched structure, each vanadium atom coordinates with six sulfur atoms by covalent bonds. Between sandwich layers, multivalent cations could diffuse conveniently. He et al. [180] synthesized VS_2 nanoflowers and the VS_2/Zn system (electrolyte: 1 M $ZnSO_4$) delivers a capacity of 190.3 mAh g^{-1} at a current density of 0.05 A g^{-1}. Ninety-eight percentage of capacity could be obtained after 200 cycles at 0.5 A g^{-1} (Fig. 7d). However, the operating voltages of chalcogenides are usually low (< 0.6 V vs. Zn/Zn^{2+}). It is vital for a cathode material to deliver relatively high voltage if high power density is required. The voltage window of VS_2 is only 0.4–1 V, which is lower than that of other reported vanadium-based compounds (Fig. 7e). The operation mechanism of VS_2/Zn system is based on intercalation reaction, which has been demonstrated by ex situ XRD analysis and HRTEM pattern. The variation of lattice spacing of (002) could be directly observed in HRTEM images (Fig. 7f). When discharge happens, Zn ions are inserted into cathode, and d_{002} increases by 1.73%, in accordance with intercalation mechanism.

Hollandite-type vanadium oxide owns a typical chemical formula of $A_xV_8O_{16}$, in which "A" denotes metal cations. Jo et al. [181] firstly focused on the insertion of Zn^{2+} ions into this crystal structures. In this work, they investigated a tunnel-structured hollandite-type $VO_{1.52}(OH)_{0.77}$ as cathode material for RZBs. Al doping is an effective method to stabilize crystal structure, and it has been confirmed in some studies of cathode materials for Li-ion batteries, such like $LiCoO_2$ and $LiNiO_2$ [182]. Therefore, cathodes that utilize Al-doped materials might exhibit improved electrochemical performances. Jo et al. further synthesized the Al-doped $VO_{1.52}(OH)_{0.77}$, in which Al preferred to replace V^{3+}, resulting in the increase of average oxidation state of V when the Al content increased in $V_{1-x}Al_xO_{1.52}(OH)_{0.77}$. The Al-doped structures of bare $VO_{1.52}(OH)_{0.77}$ are shown in Fig. 7g. Two distorted VO_6 octahedra share an edge which orients parallel to c axis. The contact angle of O–V–O in these octahedra is approximately 168°, resulting in difference of lengths between V and each O. Eight octahedra could form a [2×2] tunnel and each edge of this square shape tunnel consists of two VO_6 octahedra. The diameter of this hollandite-type tunnel is approximately 5.5 Å, which is large enough to accommodate the intercalation of Zn^{2+} ions. The Al-doping method could further stabilize this structure, owing to the presence of strong Al–O bonds. The researcher found that different Al doping proportions lead to different electrochemical performances. The non-doped sample ($x = 0$) exhibits poor cycling stability, its capacity decreases a lot after 5 cycles. The Al-doped samples ($x = 0.05$ and $x = 0.09$) deliver better cycling performance (Fig. 7h). The capacity fading during initial 5 cycles is efficiently restrained,

and the remaining capacities are higher than that of non-doped sample. Notably, the enhancement of electrochemical performance and the ratio of Al-doping are not in direct proportion, because the capacity of $V_{0.95}Al_{0.05}O_{1.52}(OH)_{0.77}$ is higher than $V_{0.91}Al_{0.09}O_{1.52}(OH)_{0.77}$. The schema of reaction mechanism is shown in Fig. 7i, which illustrates (de)intercalation of Zn^{2+} ions (out of) into the $V_{1-x}Al_xO_{1.52}(OH)_{0.77}$ ($x = 0$–0.09) tunnel structure. After discharge process, 2 of 4 hydrogen atoms in each tunnel are replaced by zinc atoms, which is a reversible reaction in the whole charge/discharge process. Doping method could unlock the electrochemical activity of cathode materials. This general strategy could introduce the new available vacant sites and improve the thermodynamical driving force of diffusion cations. In addition, kinetic limitation of diffusion for multivalent cations can be removed with higher concentration of vacancies. Inevitably, doping strategy will decrease the theoretical maximum capacity of cathode materials because partial redox-active transition metal centers will disappear.

4 Vanadium-Based Compounds for Rechargeable Aluminum Battery System

Al metal is used as anode directly in RABs, achieving three-electron redox reaction. Up to now, the common ionic electrolyte is $AlCl_3$ imidazolium-based chloride, which can deliver Al^{3+} or $AlCl_4^-$ efficiently. Regardless of the breakthrough in recent years, RABs still require further explorations about electrolyte and cathode materials. At present, the development of RABs mostly relies on the layered graphite materials, which provide fast ion diffusion channels and stable cycling performance. Similar to the typical layered graphite structure, the vanadium-based material of V_2O_5 is widely implemented in RABs and has greatly improved the performance of RABs. The following derivative vanadium-based materials, such as VS_4 and V_2CT_x, also exhibit good electrochemical performance. Except the layered structure, electrochemical behaviors of NASICON and other kinds of vanadium-based materials have also been investigated. The influence of structure and detailed reaction mechanism will be explained in the following content.

4.1 Vanadium Oxides

V_2O_5 was used as cathode material in RABs firstly by Jayaprakash et al. [86]. They used the nonaqueous electrolyte, which was a composite of $AlCl_3$ and [EMIm]Cl with molar ratio of 1.1:1, and the V_2O_5 nanowires cathode material was prepared via hydrothermal method. With the

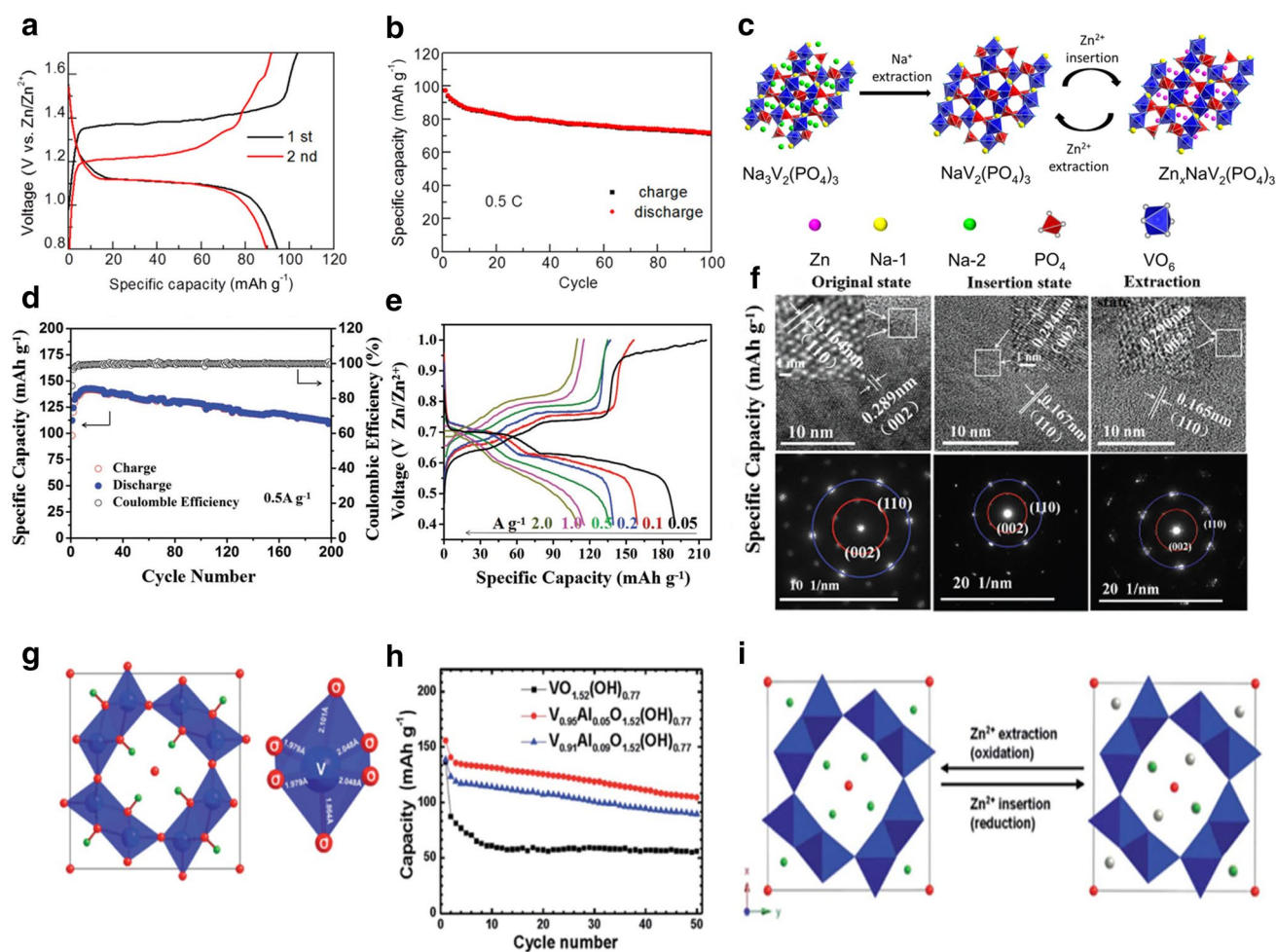**Fig. 7** **a** Galvanostatic charge–discharge curves and **b** cycling performance of $Na_3V_2(PO_4)_3$ at a current density of 50 mA g^{-1}. **c** schematic representation for phase transition of $Na_3V_2(PO_4)_3$ cathode during cycling. Figure **a**–**c** reproduced with permission [177]. Copyright 2016, Elsevier. **d** Long-term cyclic properties of VS_2 at a current density of 0.5 A g^{-1}. **e** charge and discharge curves of VS_2 at the current density from 0.05 to 2.0 A g^{-1}. **f** HRTEM images and SAED patterns of VS_2 at original, insertion and extraction states.
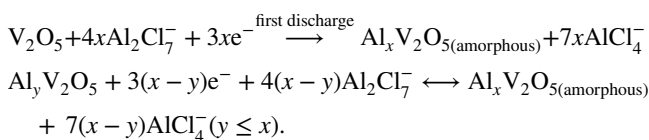
Figure **d**–**f** reproduced with permission [180]. Copyright 2017, WILEY–VCH. **g** the Al-doped structures of $VO_{1.52}(OH)_{0.77}$. **h** the cycling performance of $VO_{1.52}(OH)_{0.77}$, $V_{0.95}Al_{0.05}O_{1.52}(OH)_{0.77}$ and $V_{0.91}Al_{0.09}O_{1.52}(OH)_{0.77}$. **i** Zn^{2+} ions intercalation/de-intercalation process in the $V_{1-x}Al_xO_{1.52}(OH)_{0.77}$ ($x = 0$–0.09) tunnel model structure. Figure **g**–**i** reproduced with permission [181]. Copyright 2017, Royal Society of Chemistry

orthorhombic crystal structure, V_2O_5 can achieve reversible insertion and extraction of the Al^{3+} ions. They coated the active materials on the stainless steel current collector and assembled coin-type cell [86]. As a result, the discharge voltage plateau of V_2O_5 is around 0.55 V. The initial discharge capacity of 305 mAh g^{-1} is obtained at the current density of 125 mA g^{-1} (Fig. 8a). 0.7 mol Al^{3+} ions might intercalate into the materials, which is lower than the theoretical capacity of 442 mAh g^{-1} (1 mol Al^{3+} ions participate in the discharge process) [86]. After 20 cycles, the specific capacity decreases to 273 mAh g^{-1} (Fig. 8b). On the contrary, Reed et al. [183] indicated that with the increasing ratio of active materials (V_2O_5) in the cathode,

the electrochemical performance of Al^{3+} ions storage will obviously get worse. When they used stainless steel as current collector, the cell delivered a certain electrochemical activity. However, when the stainless steel was replaced by platinum current collector, there was no obvious electrochemical activity. The results illustrate that the V_2O_5 might have no electrochemical activity and even has detrimental influence on Al^{3+} ions storage. Actual capacity might come from the reaction between acid electrolyte and iron/chromium in stainless steel current collector. Nevertheless, there is no sufficient characterization method to illustrate the specific reaction between the stainless steel current and electrolyte.

To avoid the corrosion of the stainless steel, Wang et al. [184] introduced a method of combining the cathode materials with current collector directly through depositing V_2O_5 on a Ni-foam substrate. As a result, the well-distributed V_2O_5 particles on the surface of 3D porous structure performed the capacity of 239 mAh g^{-1} at the current density of 44.2 mA g^{-1}. Moreover, the different kinds of binders also have impact on the electrochemistry performance. In electrolyte AlCl$_3$/[BMIM]Cl (mole ratio 1.1:1) ionic liquid, V_2O_5 nanowire cathode with polyvinylidene fluoride (PVDF) binder was utilized as the control sample. As a result, the cathode with the polytetrafluoroethylene (PTFE) binder showed higher voltage plateaus and capacity. The initial discharge capacity of the V_2O_5 nanowires with PTFE was 86.5 mAh g^{-1} at 44.2 mA g^{-1}. The different electrical conductivities of binders might explain the differences of electrochemical performances. As expected, the performance of binder-free V_2O_5 was superior to these materials at the same current density [184].

The deep study of V_2O_5 as cathode material in RABs was reported recently by Gu et al. [185]. They proposed that the Al^{3+} ions storage process in V_2O_5 is accompanied by structural transformation, the amorphous layer is also formed on the surface of V_2O_5 nanowires in the first discharge process. The schematic diagram is shown in Fig. 8c. The process of Al^{3+} ions insertion into the V_2O_5 nanowires can be divided into two steps. Firstly, Al^{3+} ions combine with AlCl$_4^-$ (Al^{3+}+7AlCl$_4^- \rightarrow$ 4Al$_2$Cl$_7^-$) and the Al$_2$Cl$_7^-$ is irreversibly inserted into the layer of V_2O_5. Then, during the reversible cycling process, phase transition will emerge on the surface of V_2O_5 nanowires and Al^{3+} ions will be reversibly inserted into the cathode simultaneously. The reaction takes place as given in the following formulae:

$$V_2O_5 + 4xAl_2Cl_7^- + 3xe^- \xrightarrow{\text{first discharge}} Al_xV_2O_{5(\text{amorphous})} + 7xAlCl_4^-$$

$$Al_yV_2O_5 + 3(x-y)e^- + 4(x-y)Al_2Cl_7^- \longleftrightarrow Al_xV_2O_{5(\text{amorphous})}$$
$$+ 7(x-y)AlCl_4^- (y \leq x).$$

As shown in the above equations, the theoretical value of the first discharge capacity is estimated to be 106 mAh g^{-1}, which is consistent with measured discharge capacity (107 mAh g^{-1}). But after one cycle, only 53.4 mAh g^{-1} capacity remains. These phenomena can be explained through the ex situ XPS and XRD (Fig. 8d, e). From the result, there exists a slight amount of V^{3+} after the first charge process (disproportionation reaction might occur in this process, V$^{4+} \rightarrow$ V^{5+}+V^{3+}), indicating not all of V^{4+} reverts to V^{5+} during the charge process [185]. In addition, it is discovered that the average valance state of discharged V_2O_5 after 10 cycles is higher than that in the first cycle. The reason for this phenomenon is that few Al^{3+} ions might remain in the crystal structure of V_2O_5, leading to the recession of the capacity. In the ex situ XRD (Fig. 8e), the split of (101) peak explains the irreversibly phase transition in the first cycle [185]. This result also account for the capacity decay. On the other hand, the reversible changes of the (001) peak illustrate the reversible phase transition process of V_2O_5 in 5th and 10th cycles (Fig. 8f). In summary, the detailed ex situ XRD and XPS characterizations contribute to prove the intercalation process of Al^{3+} ions. However, there still exist some drawbacks in the research, e.g., the XPS only detects the surface information of cathode, which might lead to false conclusions.

To improve the electrochemical performance of V_2O_5, Chiku et al. [186] adopted V_2O_5/C composites and new electrolyte. In their work, the electrolyte is mixed solution of aluminum chloride, dipropylsulfone and toluene (1:10:5 in mole ratio) [186]. The toluene is an additive, which can improve the viscosity and has no influence on the Al deposition. But the underlying mechanism is still unknown [187]. Moreover, the three components in electrolyte are more stable and suitable for Mo current collector, which effectively improve the cycling life and initial capacity of battery. The first discharge capacity of V_2O_5/C in this system is approximately 150 mAh g^{-1} at 22.1 mA g^{-1} (Fig. 8g) [186]. However, the V_2O_5/C is not stable at low current density. When charge/discharge at higher current density of 44.2 mA g^{-1}, the capacity of V_2O_5/C is 50 mAh g^{-1} and nearly 90% capacity remains after 30 cycles (Fig. 8h). The vanadium reduction is accompanied by Al^{3+} ions insertion, and the structure will be destroyed when Al^{3+} ions intercalation arrives at a certain level. According to XPS results, the reaction of V_2O_5 is not complete. In the first discharge progress, the valence state of the V^{5+} reduces to V^{3+} and V^{4+}. After the next charge process, the percentage of the V^{5+} is only 91%, and the content of V^{4+} is 9% [186]. This phenomenon that part of V^{4+} cannot return to V^{5+} state also explains the reason for the decreasing of the capacity. The modification of V_2O_5 with simply physical composition is not the fundamental solution to overcome the problem of poor cycling stability and capacity decay. Thus, a new approach to modify V_2O_5 is required. For instance, we can adopt doping method, such as the work about TiO$_2$ [188]. Through the doping method, the high concentration of Ti^{4+} vacancies can increase the reversible capacity in RABs.

In order to break through the limitation of cycling life, many researchers focused on the exploration of new electrolyte. Wang et al. [189] used a new electrolyte which consisted of Al(OTF)$_3$/[BMIM]OTF ionic liquids and maintained the synthesis process of V_2O_5 similar to their previous work. In contrast to other electrolyte system, the novel electrolyte performed high decomposition potential (3.25 V vs. Al/Al^{3+}) and conductivity, relying on the high aggregation of anion group OTF$^-$ with Al^{3+} ions. There is a similar work
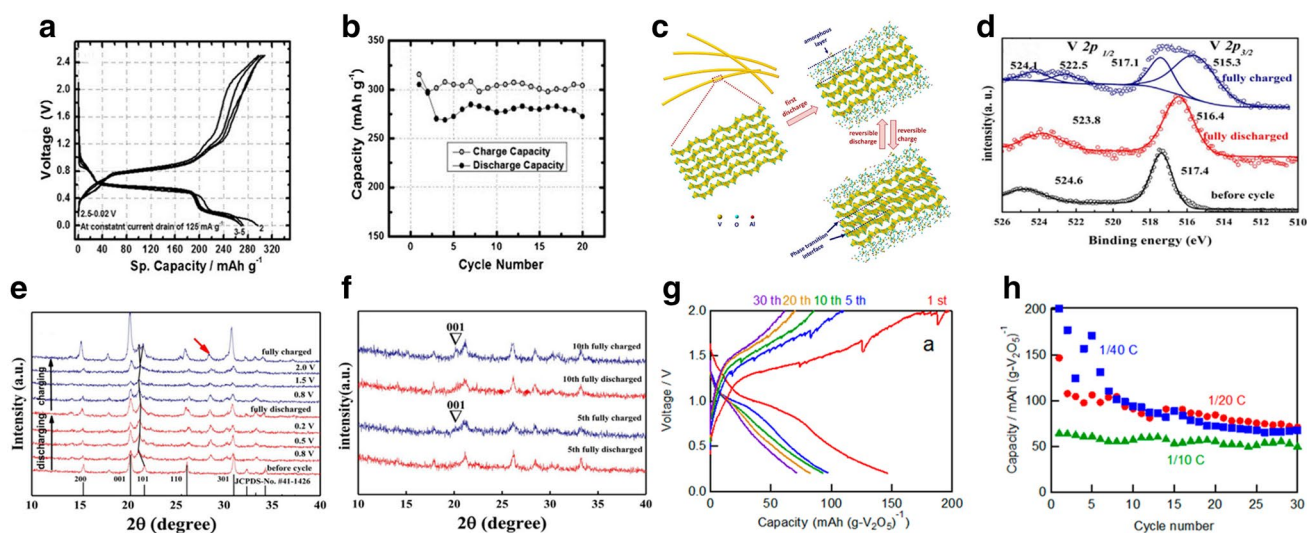
Fig. 8 a Galvanostatic charge–discharge curves and **b** cycling performance of V_2O_5 at current density of 125 mA g^{-1}. Figure **a**, **b** reproduced with permission [86]. Copyright 2011, Royal Society of Chemistry, **c** schematic diagram of Al^{3+} electrochemical insertion/extraction in crystallized V_2O_5 nanowire. **d** ex situ XPS patterns and **e** XRD patterns of V_2O_5 cathode at various discharge and charge states through the first cycle. **f** ex situ XRD patterns of V_2O_5 cathode after the 5th and 10th discharge and charge. Figure **c**–**f** reproduced with permission [185]. Copyright 2016, Elsevier. **g** galvanostatic charge–discharge curves and **h** cycling performance of V_2O_5/C at different current densities. Figure **g**, **h** reproduced with permission [186]. Copyright 2015, American Chemical Society

reported by Wang et al. [190]. They found that different mole ratio of anionic groups in electrolyte could have great effect on the electrochemical performance [190]. When the $[BMIm]^+$ combines with $[AlCl_4]^-$, the lowest highest occupied molecular orbital (HOMO) energy has been shown in the calculation result by DFT, which might provide higher electrochemical activity [190]. Gonzalez et al. [191] also reported the shield effect of water molecules on Al^{3+} ions in aqueous electrolyte (1 M $AlCl_3$ dissolve in deionized water). In this system, V_2O_5 delivers the initial capacity of about 120 mAh g^{-1} at a current density of 60 mA g^{-1}. But the cycling number is limited within 14 cycles.

Wang et al. [192] first reported the VO_2 as cathode material in RABs. The VO_2 possesses four channels for Al^{3+} ions diffusion. Based on the crystal structure of VO_2, the authors introduced computational simulations to investigate the formation energy and the change of cell volume during intercalation of Al^{3+} ions. When these channels accommodate over two Al^{3+} ions, the V–O bonds are deemed to be broken and an irreversible expansion of cell volume will occur (Fig. 9a–f). According to the variations of formation energies and cell volumes at different ratios of Al^{3+} ions in VO_2, a stable and feasible reaction needs two conditions: low formation energy and slight change of the cell volume. To satisfy these two requirements, only when two Al^{3+} ions intercalate into channels exactly will the VO_2 crystal structure remain relatively stable. Then, they synthesized VO_2 nanorods and the initial discharge capacity of 165 mAh g^{-1} is obtained at the current density of 50 mA g^{-1} (Fig. 9g).

After 100 cycles, ~70% capacity is retained. At relative high current density of 100 and 200 mA g^{-1}, the VO_2 nanorods still possess the capacity of 106 and 70 mAh g^{-1} after 100 cycles (Fig. 9h), respectively. This work explicitly demonstrated the reversible Al^{3+} ions storage mechanism in VO_2 by computational simulations. The authors also synthesized VO_2 nanorods, which exhibited a good electrochemical performance in RABs. But there still exist some drawbacks of VO_2, such as low voltage plateaus and unsatisfactory cycling performances. Moreover, whether stainless steel current collector participates in the reaction still remains controversial.

4.2 Other Vanadium-Based Materials

Li_3VO_4 is an attractive anode material in Li-ion batteries, due to its crystal structure that is composed of VO_4 and LiO_4 tetrahedrons, which could achieve reversible (de)intercalation of Li^+ ions accompanied by high diffusion rate [193]. However, some obstacles also need to be overcome, such as the poor electronic conductivity, which dictate the deteriorative rate performance. Modification with graphene or carbon nanotubes is a feasible method to enhance the electronic conductivity [193, 194]. Jiang et al. [195] fabricated the hollow sphere Li_3VO_4/C via spray drying process and assembled it in RABs. The novel synthesis method formed mesoporous sphere whose size was about 0.5–10 μm, and carbon layer was well distributed on the surface of the sphere. Based on the mesoporous sphere morphology and carbon layer, the electronic conductivity of Li_3VO_4 could be improved much.

Combining the first principle calculation with XRD analysis, the free energy at a sites (− 4.35 eV) is lower than that at b sites (− 3.22 eV). During Al^{3+} ions insertion in the a sites, all lattice parameter changes are 0.1 Å, which approaches the calculated results (Fig. 10a–c). The novel Li_3VO_4/C cathode materials in RABs exhibit a good electrochemistry performance and obvious reversible redox peaks (Fig. 10d). The high discharge/charge capacity of 137/85 mAh g^{-1} can be obtained in the first cycle (Fig. 10e). After 100 cycles, the reversible capacity is nearly 48 mAh g^{-1} and the coulombic efficiency is approximately 100% (Fig. 10f). From the ex situ XRD result, in the first discharge process, the d space of Li_3VO_4 will increase about 0.03 Å and the diffraction peak intensities reduce slowly with the ongoing discharge process. In this process, a slight distortion of crystal structure might accommodate the intercalation of Al^{3+} ions. In the charge process, the diffraction peak intensities recover a little but are still lower than those of the original electrodes. After 70 cycles, the crystallinity of cycled Li_3VO_4 decreases and the displacement distance of d space still exists. The repeated Al^{3+} ions insertion/extraction might lead to the accumulation of crystallinity decrease, which accounts for the capacity decay of Li_3VO_4. On the other hand, its voltage plateaus (0.37 and 0.81 V vs. Al/Al^{3+} in the discharge and charge process) are lower than those of most vanadium-based materials in RABs because of the inherent property of Li_3VO_4 (average voltage below 1.0 V vs. Li/Li$^+$), leading to the limitation of energy density. In spite of the imperfect electrochemical performance, optimizing Al^{3+} ions storage performance in the vanadate-based cathode materials is realized for the first time. On the other hand, in-depth exploration and modification in the vanadate-based cathode materials are still needed.

Vanadium-based NASICONs are also potential materials in RABs [196, 197]. Recently, Nacimiento et al. [196] reported $Na_3V_2(PO_4)_3$ as cathode material in RABs. The authors applied the aqueous electrolyte (0.1 M AlCl$_3$ in deionized water) in RABs to achieve the storage of Al^{3+} ions. All the electrochemical tests were measured in three-electrode system, in which the Pt and Ag/AgCl electrodes acted as counter and reference electrodes, respectively. The $Na_3V_2(PO_4)_3$ could deliver the capacity of ~ 100 mAh g^{-1} at current density of 60 mA g^{-1}. After 20 cycles, only ~ 35% capacity remained. The reasons for the capacity decay are the partial dissolution and structure degradation of the cathode material. From the ICP, NMR, XPS and XRD results, 1.9 mol Na$^+$ ions will be extracted from $Na_3V_2(PO_4)_3$ per formula unit during first charge process and 0.3 mol Al^{3+} ions will be inserted into material during the discharge process. Due to the replacement of Al^{3+} to Na$^+$ ions, the formation of Al–O bonds will weaken the Na–O bonds, which destroys the structure stability. In the cycling process, both bulk insertion and surface capacitance are detected. The authors also thought that a slight amount of protons will be

inserted into materials. Then, they assembled $Na_3V_2(PO_4)_3$ cathode in RABs with nonaqueous electrolyte. Reversible capacity of 60–70 mAh g^{-1} was obtained with a plateau of ~ 1.25 V, which is similar to the related work result of Sun et al. [197]. But the reaction mechanism is still unclear in the organic electrolyte.

Transition metal carbides (MXene), as one of the members of 2D materials, possesses high surface areas, high conductivity and excellent theoretical specific capacity [198]. Recently, Armin et al. adopted layered vanadium carbide MXene (V_2CT_x) as cathode materials in the RABs (Fig. 11a) [199]. In AlCl$_3$/[EMIm]Cl electrolyte, V_2CT_x shows a high average discharge voltage of ~ 1.2 V (vs. Al/Al^{3+}) and delivers high specific capacity of ~ 330 mAh g^{-1} at current density of 10 mA g^{-1} (Fig. 11b). From the ex situ XRD and HRTEM results, the increase in the interlayer distance of about 0.10 Å was detected in the first discharge process and interlayer space remained stable in the subsequent cycling process. According to ionic size, Al^{3+} ions were the main species intercalated rather than [AlCl$_4$]$^-$, [Al$_2$Cl$_7$]$^-$ or EMI$^+$ in the cycling process. On the other hand, EDS result also detected large increase in Al element in V_2CT_x after
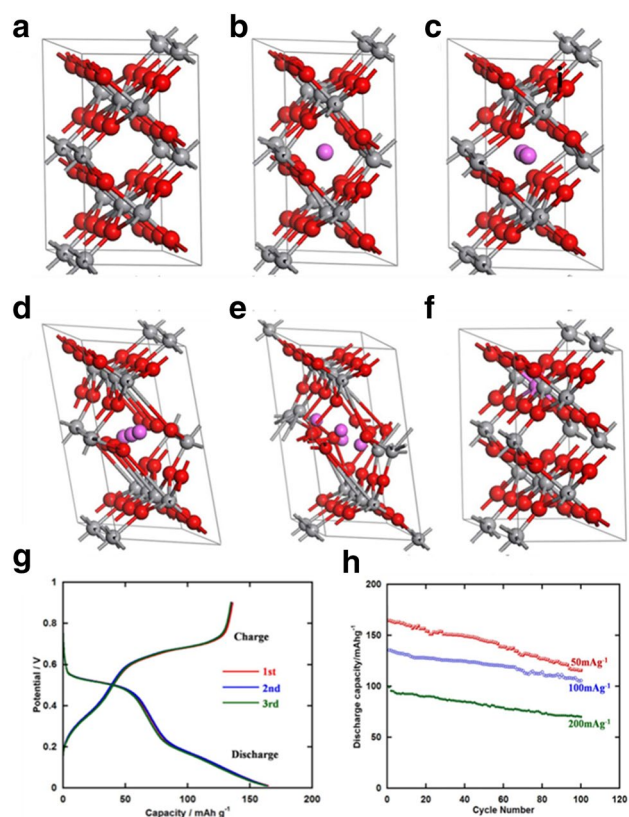

Fig. 9 a–e The various number of Al atomic (0, 1, 2, 3, 4) in [(V_4O_8)($V_{12}O_{24}$)]. **f** the structure of AlV$_{15}$O$_{32}$. **g** the charge/discharge curves of VO$_2$ at the current density of 50 mA g^{-1}. **h** cycling performance of VO$_2$ at different current density. Figure **a–h** reproduced with permission [192]. Copyright 2013, Springer

discharge, but only a small amount of Cl element existed in V_2CT_x at the same state. The authors hypothesized that the repulsion effect between negatively charged V_2CT_x surfaces will be reduced by Al^{3+} ions intercalation, which will result a very small change in the interlayer spacing. To improve the electrochemical performance of V_2CT_x, the authors synthesized the few-layered V_2CT_x (FL-V_2CT_x) and TBAOH-assisted delamination V_2CT_x (TBAOH-FL-V_2CT_x), which decreased the particle size and energy barrier for the diffusion of Al^{3+} ions. Although these enhanced V_2CT_x showed much higher capacity and excellent rate performance, the rapid capacity decay still exist in initial cycles. Alleviating the capacity decay problem and controlling the surface chemistry of V_2CT_x are important to the further improvement of electrochemical performance.

Recently, Zhang et al. [200] reported flower-like VS$_4$/rGO composite applied in RABs. At 100 mA g^{-1}, VS$_4$/rGO could deliver a high initial specific capacity of 406.94 mAh g^{-1} (Fig. 11c). But its capacity decreased rapidly to 80 mAh g^{-1} in the first 20 cycles and stabilized at the ~ 80 mAh g^{-1} over 100 cycles (Fig. 11d). The authors further investigated the electrochemical mechanism in the cycling process. XPS results illustrated that valence states of vanadium and sulfur elements were changed in the cycling process. From Raman result, the intensity ratios of D/G (I_D/I_G) improved after change process (1.123 for charging state and 1.081 for discharging state). This increased ratio might result from the increased edge planes, disorder degree and the size reduction of sp^2 domain in composites. The shrinkage of the thickness of VS$_4$/rGO after being charged to 2 V was also found from atomic force microscope (AFM) images. In this work, morphology change of VS$_4$/rGO in cycling process was studied in detail, and cycling performance of VS$_4$/rGO could remain stable at ~ 80 mAh g^{-1} for 100 cycles. However, the reason of rapid decrease in specific capacity in the first 20 cycles and the insertion mechanism of Al^{3+} ions are still unclear.

5 Conclusions and Future Outlook

This review has included the progress of the vanadium-based cathode materials in rechargeable multivalent batteries. Rechargeable multivalent batteries are still attractive alternatives to Li-ion batteries because of high security, low price and high energy density. On the other hand, vanadium-based compounds are the appropriate cathode materials owning to the unique properties. However, there are many problems which need to be resolved. Firstly, present research about compatible electrolyte which could steadily transport the multivalent cations with wide voltage window is still unsatisfactory and suffers slow progress. The present electrolytes limit the development of cathode materials seriously. Secondly, although state-of-the-art multivalent batteries could cycle more than 1000 times and possess high specific capacity (> 300 mAh g^{-1}) owing to the variable chemical valences of vanadium, the low operating voltage still limits the further
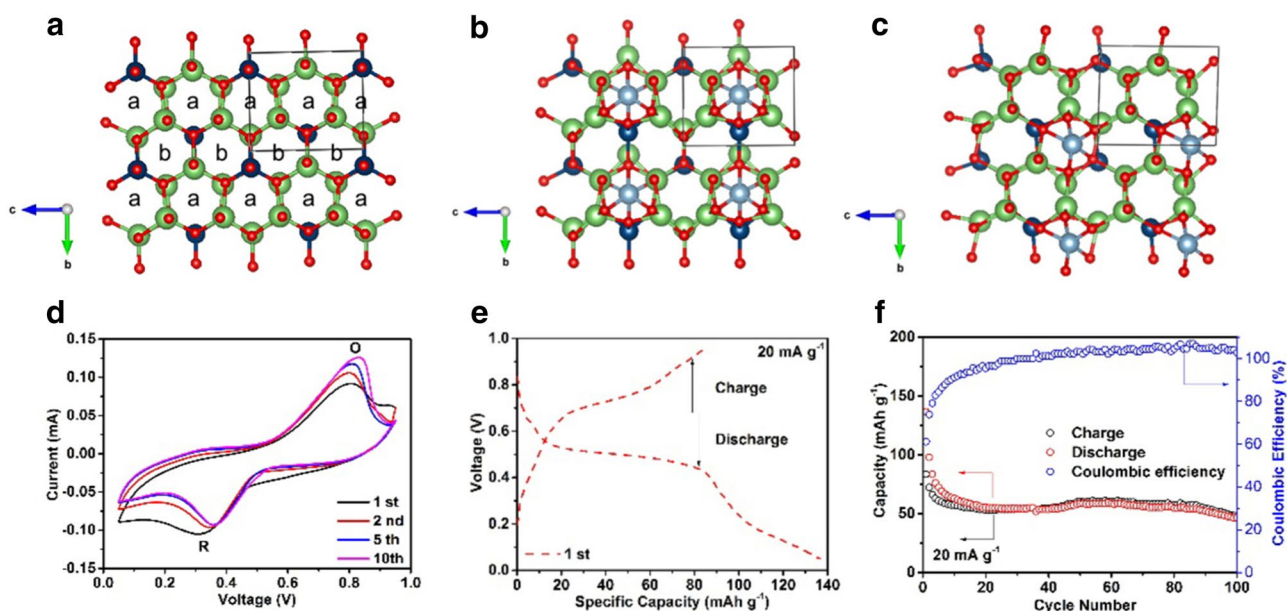

Fig. 10 The crystal structures of Al$_x$Li$_3$VO$_4$ projected along *a* axis. **a** Initial Li$_3$VO$_4$, with a-site and b-site to accommodate Al insertion. Ball and stick model of Li$_3$VO$_4$ with Al inserted into **b** a-site and **c** b-site. Color code: Li, green; V, dark blue; O, red; Al: light blue. **d** cyclic voltammogram of Li$_3$VO$_4$ at the scan rate of 0.1 mV s^{-1}. **e** the initial charge and discharge curves of Li$_3$VO$_4$ at the current density of 20 mA g^{-1}. **f** cycling performance and coulombic efficiency of Li$_3$VO$_4$ at a current density of 20 mA g^{-1}. Figure **a**–**f** reproduced with permission [195]. Copyright 2017, American Chemical Society

Fig. 11 a Schematic illustration of the proposed mechanism for an Al-battery with V_2CT_x MXene as the cathode during discharge in $AlCl_3$:[EMIm]Cl (1.3:1) ionic liquid electrolyte. **b** Galvanostatic charge–discharge curves of V_2CT_x cathode at current density of 10 mA g^{-1}. Figure **a**, **b** reproduced with permission [199]. Copyright 2017, American Chemical Society. **c** the charge–discharge curves of VS_4/rGO composite cathode at the current density of 100 mA g^{-1}. **d** The histogram of cycling performances of VS_4/rGO composite at a current density of 100 mA g^{-1} from the 10th to 100th cycle (per 10 cycles). Figure **c**, **d** reproduced with permission [200]. Copyright 2018, WILEY–VCH
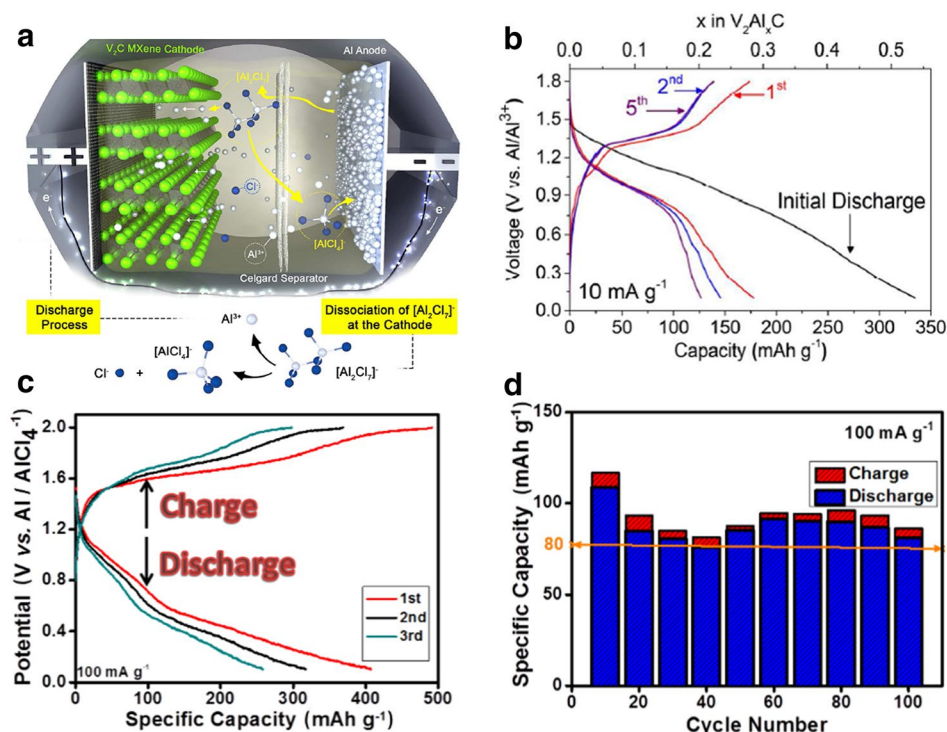
development of practical application. Inevitably, the higher reduction potential of multivalent metal (− 2.356 V of Mg, − 0.763 V of Zn and − 1.66 V of Al vs. standard hydrogen electrode) compared with lithium (− 3.07 V vs. standard hydrogen electrode) decrease the operating voltage further. Finally, due to the facile distortion of V–O octahedra and intensely polarization effect of multivalent cations, part of vanadium-based materials still suffer the poor cycling stability. The ideal vanadium-based materials that could provide flexible channel for multivalent cations diffusion and possess stable crystal structure simultaneously are the development direction of future research.

Scientific breakthroughs about multivalent batteries have been reported with increasing rate in last 10 years. Although many problems remain to be solved and the large gap in electrochemical performance between multivalent batteries and Li-ion batteries still exists, unique advantage of multivalent metals and the resource scarcity problem of lithium stimulate the researchers constantly to lucubrate the new types of high-performance multivalent batteries. Theoretically, vanadium-based materials with rich chemical valences are the appropriate candidates as cathode materials in multivalent batteries. However, a large amount of efforts are still needed to achieve the prospective target. Effective strategies should be proposed to optimize the crystal structure and promote the electrochemically intercalated/deintercalated process in the future. The conventional optimization strategies borrowed from Li-ion battery, such as nanocrystallization treatments to improve active surface areas, ions dopings,

carbon coatings and preparation of porous structures, have much improved the performance of vanadium-based materials. Moreover, other specific optimized methods, such as co-intercalation of water molecule or halogen, pre-intercalation strategy, amorphization treatments and controlling the multivalent cations intercalation extents, are also important to improve the electrochemical performance of vanadium-based materials. On the other hand, advanced characterization methods are important for the materials development. With the rapid progress of detection method, the intrinsic reason for many troublesome issues in vanadium-based materials will be revealed, which would guide the development of optimizing approach. After continuous exploration and innovation, we optimistically anticipate that, multivalent batteries with vanadium-based cathode materials will break through the bottlenecks in the near future.

Author Contributions The manuscript was written through contributions of all authors. All authors have given approval to the final version of the manuscript.

References

1. Dunn, B., Kamath, H., Tarascon, J.M.: Electrical energy storage for the grid: a battery of choices. Science **334**, 928–935 (2011)
2. Andre, D., Kim, S.J., Lamp, P., et al.: Future generations of cathode materials: an automotive industry perspective. J. Mater. Chem. A **3**, 6709–6732 (2015)
3. Erickson, E.M., Ghanty, C., Aurbach, D.: New horizons for conventional lithium ion battery technology. J. Phys. Chem. Lett. **5**, 3313–3324 (2014)
4. Mai, L., Yan, M., Zhao, Y.: Track batteries degrading in real time. Nature **546**, 469–470 (2017)
5. Nykvist, B., Nilsson, M.: Rapidly falling costs of battery packs for electric vehicles. Nat. Clim. Change **5**, 329–332 (2015)
6. Sakti, A., Michalek, J.J., Fuchs, E.R.H., et al.: A techno-economic analysis and optimization of Li-ion batteries for light-duty passenger vehicle electrification. J. Power Sources **273**, 966–980 (2015)
7. Whittingham, M.S.: Ultimate limits to intercalation reactions for lithium batteries. Chem. Rev. **114**, 11414–11443 (2014)
8. Yang, Z., Zhang, J., Kintner-Meyer, M.C., et al.: Electrochemical energy storage for green grid. Chem. Rev. **111**, 3577–3613 (2011)
9. Augustyn, V., Come, J., Lowe, M.A., et al.: High-rate electrochemical energy storage through Li$^+$ intercalation pseudocapacitance. Nat. Mater. **12**, 518–522 (2013)
10. Bruce, P.G., Scrosati, B., Tarascon, J.M.: Nanomaterials for rechargeable lithium batteries. Angew. Chem. Int. Ed. **47**, 2930–2946 (2008)
11. Thackeray, M.M., Wolverton, C., Isaacs, E.D.: Electrical energy storage for transportation—approaching the limits of, and going beyond, lithium-ion batteries. Energy Environ. Sci. **5**, 7854–7863 (2012)
12. Ruth, M.F., Zinaman, O.R., Antkowiak, M., et al.: Nuclear-renewable hybrid energy systems: opportunities, interconnections, and needs. Energy Convers. Manag. **78**, 684–694 (2014)
13. Chu, S., Majumdar, A.: Opportunities and challenges for a sustainable energy future. Nature **488**, 294–303 (2012)
14. Heller, A.: Chemical engineering challenges and investment opportunities in sustainable energy. ChemSusChem **1**, 651–652 (2008)
15. Pudukudy, M., Yaakob, Z., Mohammad, M., et al.: Renewable hydrogen economy in Asia—opportunities and challenges: an overview. Renew. Sustain. Energy Rev. **30**, 743–757 (2014)
16. Shafiei, E., Davidsdottir, B., Leaver, J., et al.: Comparative analysis of hydrogen, biofuels and electricity transitional pathways to sustainable transport in a renewable-based energy system. Energy **83**, 614–627 (2015)
17. Abruna, H.D., Kiya, Y., Henderson, J.C.: Batteries and electrochemical capacitors. Phys. Today **61**, 43–47 (2008)
18. Crowther, O., West, A.C.: Effect of electrolyte composition on lithium dendrite growth. J. Electrochem. Soc. **155**, A806–A811 (2008)
19. Zhamu, A., Chen, G., Liu, C., et al.: Reviving rechargeable lithium metal batteries: enabling next-generation high-energy and high-power cells. Energy Environ. Sci. **5**, 5701–5707 (2012)
20. Crabtree, G.: The joint center for energy storage research: a new paradigm for battery research and development. In: Physics of Sustainable Energy III (PSE III): Using Energy Efficiently and Producing It Renewably, 3rd Physics of Sustainable Energy (PSE) Conference, Berkeley, March 2014. AIP Conference Proceedings, vol. 1652, pp. 112–128. American Institute of Physics, Melville (2015)
21. Berg, E.J., Villevieille, C., Streich, D., et al.: Rechargeable batteries: grasping for the limits of chemistry. J. Electrochem. Soc. **162**, A2468–A2475 (2015)
22. Eroglu, D., Ha, S., Gallagher, K.G.: Fraction of the theoretical specific energy achieved on pack level for hypothetical battery chemistries. J. Power Sources **267**, 14–19 (2014)
23. Gallagher, K.G., Goebel, S., Greszler, T., et al.: Quantifying the promise of lithium-air batteries for electric vehicles. Energy Environ. Sci. **7**, 1555–1563 (2014)
24. Gallagher, K.G., Nelson, P.A., Dees, D.W.: Simplified calculation of the area specific impedance for battery design. J. Power Sources **196**, 2289–2297 (2011)
25. Gallagher, K.G., Trask, S.E., Bauer, C., et al.: Optimizing areal capacities through understanding the limitations of lithium-ion electrodes. J. Electrochem. Soc. **163**, A138–A149 (2016)
26. Lu, X., Kirby, B.W., Xu, W., et al.: Advanced intermediate-temperature Na–S battery. Energy Environ. Sci. **6**, 299–306 (2012)
27. Lu, X., Lemmon, J.P., Kim, J.Y., et al.: High energy density Na–S/NiCl$_2$ hybrid battery. J. Power Sources **224**, 312–316 (2013)
28. Manwell, J.F., Mcgowan, J.G.: Lead acid battery storage model for hybrid energy systems. Sol. Energy **50**, 399–405 (1993)
29. Abruna, H.D., Goodenough, J.B., Buchanan, M.V.: ANYL 28-Summary overview of basic research needs for electrical energy storage. In: Abstracts of Papers of the American Chemical Society, vol. 234, 28-ANYL. American Chemical Society, Washington, DC (2007)
30. Iwase, S., Minato, T.: Lead acid battery, has container, cover with exhaust port and projection disposed on peripheral portion of exhaust port that is formed in upper or side surface of cover. US Patent 2003049521-A1, 13 Mar 2003
31. Saiju, R., Heier, S.: Performance analysis of lead acid battery model for hybrid power system. In: 2008 IEEE/PES Transmission and Distribution Conference & Exposition, Chicago, April 2008. pp. 404-409. IEEE, Piscataway (2008)
32. Nogueira, C.A., Delmas, F.: New flowsheet for the recovery of cadmium, cobalt and nickel from spent Ni–Cd batteries by solvent extraction. Hydrometallurgy **52**, 267–287 (1999)
33. Reddy, B.R., Priya, D.N., Rao, S.V., et al.: Solvent extraction and separation of Cd(II), Ni(II) and Co(II) from chloride leach liquors of spent Ni–Cd batteries using commercial organo-phosphorus extractants. Hydrometallurgy **77**, 253–261 (2005)
34. Sun, B., Skyllas-Kazacos, M.: Modification of graphite electrode materials for vanadium redox flow battery application—I. Thermal treatment. Electrochim. Acta **37**, 1253–1260 (1992)
35. Liu, Q.H., Grim, G.M., Papandrew, A.B., et al.: High performance vanadium redox flow batteries with optimized electrode configuration and membrane selection. J. Electrochem. Soc. **159**, A1246–A1252 (2012)
36. Sun, B., Skyllas-Kazacos, M.: Chemical modification of graphite electrode materials for vanadium redox flow battery application. Part II. Acid treatments. Electrochim. Acta. **37**, 2459–2465 (1992)
37. Jian, Z., Han, W., Liang, Y., et al.: Carbon-coated rhombohedral Li$_3$V$_2$(PO$_4$)$_3$ as both cathode and anode materials for lithium-ion batteries: electrochemical performance and lithium storage mechanism. J. Mater. Chem. A **2**, 20231–20236 (2014)
38. Song, W., Ji, X., Pan, C., et al.: A Na$_3$V$_2$(PO$_4$)$_3$ cathode material for use in hybrid lithium ion batteries. Phys. Chem. Chem. Phys. **15**, 14357–14363 (2013)
39. Song, W., Ji, X., Yao, Y., et al.: A promising Na$_3$V$_2$(PO$_4$)$_3$ cathode for use in the construction of high energy batteries. Phys. Chem. Chem. Phys. **16**, 3055–3061 (2014)
40. Liu, J., Zhang, J.G., Yang, Z., et al.: Materials science and materials chemistry for large scale electrochemical energy storage:

from transportation to electrical grid. Adv. Funct. Mater. **23**, 929–946 (2013)

41. Plashnitsa, L.S., Kobayashi, E., Noguchi, Y., et al.: Performance of NASICON symmetric cell with ionic liquid electrolyte. J. Electrochem. Soc. **157**, A536–A543 (2010)

42. Yao, Y., Mcdowell, M.T., Ryu, I., et al.: Interconnected silicon hollow nanospheres for lithium-ion battery anodes with long cycle life. Nano Lett. **11**, 2949–2954 (2011)

43. Fergus, J.W.: Recent developments in cathode materials for lithium ion batteries. J. Power Sources **195**, 939–954 (2010)

44. He, C., Wu, S., Zhao, N., et al.: Carbon-encapsulated Fe_3O_4 nanoparticles as a high-rate lithium ion battery anode material. ACS Nano **7**, 4459–4469 (2013)

45. Canepa, P., Gautam, G.S., Hannah, D.C., et al.: Odyssey of multivalent cathode materials: open questions and future challenges. Chem. Rev. **117**, 4287–4341 (2017)

46. Massé, R.C., Uchaker, E., Cao, G.: Beyond Li-ion: electrode materials for sodium- and magnesium-ion batteries. Sci. China Mater. **58**, 715–766 (2015)

47. Levi, E., Gofer, Y., Aurbach, D.: On the way to rechargeable mg batteries: the challenge of new cathode materials. Chem. Mater. **22**, 860–868 (2010)

48. Saha, P., Datta, M.K., Velikokhatnyi, O.I., et al.: Rechargeable magnesium battery: current status and key challenges for the future. Prog. Mater. Sci. **66**, 1–86 (2014)

49. Elia, G.A., Marquardt, K., Hoeppner, K., et al.: An overview and future perspectives of aluminum batteries. Adv. Mater. **28**, 7564–7579 (2016)

50. Pan, H.L., Shao, Y.Y., Yan, P.F., et al.: Reversible aqueous zinc/manganese oxide energy storage from conversion reactions. Nat. Energy **1**, 16039 (2016)

51. Gershinsky, G., Yoo, H.D., Gofer, Y., et al.: Electrochemical and spectroscopic analysis of Mg^{2+} intercalation into thin film electrodes of layered oxides: V_2O_5 and MoO_3. Langmuir **29**, 10964–10972 (2013)

52. Aurbach, D., Weissman, I., Gofer, Y., et al.: Nonaqueous magnesium electrochemistry and its application in secondary batteries. Chem. Rec. **3**, 61–73 (2003)

53. Brissot, C., Rosso, M., Chazalviel, J.N., et al.: Dendritic growth mechanisms in lithium/polymer cells. J. Power Sources **81–82**, 925–929 (1999)

54. Shterenberg, I., Salama, M., Gofer, Y., et al.: The challenge of developing rechargeable magnesium batteries. MRS Bull. **39**, 453–460 (2014)

55. Yoo, H.D., Shterenberg, I., Gofer, Y., et al.: Mg rechargeable batteries: an on-going challenge. Energy Environ. Sci. **6**, 2265–2279 (2013)

56. Besenhard, J.O., Winter, M.: Advances in battery technology: rechargeable magnesium batteries and novel negative-electrode materials for lithium ion batteries. ChemPhysChem **3**, 155–159 (2002)

57. Cheng, Y., Liu, T., Shao, Y., et al.: Electrochemically stable cathode current collectors for rechargeable magnesium batteries. J. Mater. Chem. A **2**, 2473–2477 (2014)

58. Gregory, T.D., Hoffman, R.J., Winterton, R.C.: Nonaqueous electrochemistry of magnesium; applications to energy storage. J. Electrochem. Soc. **137**, 775–780 (1990)

59. Aurbach, D., Lu, Z., Schechter, A., et al.: Prototype systems for rechargeable magnesium batteries. Nature **407**, 724–727 (2000)

60. Gershinsky, G., Haik, O., Salitra, G., et al.: Ultra fast elemental synthesis of high yield copper Chevrel phase with high electrochemical performance. J. Solid State Chem. **188**, 50–58 (2012)

61. Levi, E., Mitelman, A., Isnard, O., et al.: Phase diagram of Mg insertion into Chevrel phases, $Mg_xMo_6T_8$ (T = S, Se). 3.

The crystal structure of triclinic $Mg_2Mo_6Se_8$. Inorg. Chem. **47**, 1975–1983 (2008)

62. Levi, M.D., Lancri, E., Levi, E., et al.: The effect of the anionic framework of Mo_6X_8 Chevrel Phase (X = S, Se) on the thermodynamics and the kinetics of the electrochemical insertion of Mg^{2+} ions. Solid State Ion. **176**, 1695–1699 (2005)

63. Mitelman, A., Levi, E., Lancry, E., et al.: On the Mg trapping mechanism in electrodes comprising Chevrel phases. ECS Trans. **3**, 109–115 (2007)

64. Mitelman, A., Levi, M.D., Lancry, E., et al.: New cathode materials for rechargeable Mg batteries: fast Mg ion transport and reversible copper extrusion in $Cu_yMo_6S_8$ compounds. Chem. Commun. **41**, 4212–4214 (2007)

65. Suresh, G.S., Levi, M.D., Aurbach, D.: Effect of chalcogen substitution in mixed $Mo_6S_{8-n}Se_n$ (n = 0, 1, 2) Chevrel phases on the thermodynamics and kinetics of reversible Mg ions insertion. Electrochim. Acta **53**, 3889–3896 (2008)

66. Tao, Z.L., Xu, L.N., Gou, X.L., et al.: TiS_2 nanotubes as the cathode materials of Mg-ion batteries. Chem. Commun. **18**, 2080–2081 (2004)

67. Arthur, T.S., Zhang, R., Ling, C., et al.: Understanding the electrochemical mechanism of K-αMnO_2 for magnesium battery cathodes. ACS Appl. Mater. Interfaces **6**, 7004–7008 (2014)

68. Huang, Z.D., Masese, T., Orikasa, Y., et al.: $MgFePO_4F$ as a feasible cathode material for magnesium batteries. J. Mater. Chem. A **2**, 11578–11582 (2014)

69. Ichitsubo, T., Adachi, T., Yagi, S., et al.: Potential positive electrodes for high-voltage magnesium-ion batteries. J. Mater. Chem. **21**, 11764–11772 (2011)

70. Kim, C., Phillips, P.J., Key, B., et al.: Direct observation of reversible magnesium ion intercalation into a spinel oxide host. Adv. Mater. **27**, 3377–3384 (2015)

71. Ling, C., Zhang, R., Arthur, T.S., et al.: How general is the conversion reaction in Mg battery cathode: a case study of the magnesiation of α-MnO_2. Chem. Mater. **27**, 5799–5807 (2015)

72. Muldoon, J., Bucur, C.B., Gregory, T.: Quest for nonaqueous multivalent secondary batteries: magnesium and beyond. Chem. Rev. **114**, 11683–11720 (2014)

73. Orikasa, Y., Masese, T., Koyama, Y., et al.: High energy density rechargeable magnesium battery using earth-abundant and non-toxic elements. Sci. Rep. **4**, 5622 (2014)

74. Wang, R.Y., Wessells, C.D., Huggins, R.A., et al.: Highly reversible open framework nanoscale electrodes for divalent ion batteries. Nano Lett. **13**, 5748–5752 (2013)

75. Zhang, R., Mizuno, F., Ling, C.: Fullerenes: non-transition metal clusters as rechargeable magnesium battery cathodes. Chem. Commun. **51**, 1108–1111 (2015)

76. Zheng, Y., Nuli, Y., Chen, Q., et al.: Magnesium cobalt silicate materials for reversible magnesium ion storage. Electrochim. Acta **66**, 75–81 (2012)

77. Aurbach, D., Gizbar, H., Schechter, A., et al.: Electrolyte solutions for rechargeable magnesium batteries based on organomagnesium chloroaluminate complexes. J. Electrochem. Soc. **149**, A115–A121 (2002)

78. Xu, C., Li, B., Du, H., et al.: Energetic zinc ion chemistry: the rechargeable zinc ion battery. Angew. Chem. Int. Ed. **51**, 933–935 (2012)

79. Mclarnon, F.R., Cairns, E.J.: The secondary alkaline zinc electrode. J. Electrochem. Soc. **138**, 645–664 (1991)

80. Lee, B., Lee, H.R., Kim, H., et al.: Elucidating the intercalation mechanism of zinc ions into α-MnO_2 for rechargeable zinc batteries. Chem. Commun. **51**, 9265–9268 (2015)

81. Alfaruqi, M.H., Mathew, V., Gim, J., et al.: Electrochemically induced structural transformation in a γ-MnO_2 cathode

of a high capacity zinc-ion battery system. Chem. Mater. **27**, 3609–3620 (2015)

82. Hertzberg, B.J., Huang, A., Hsieh, A., et al.: Effect of multiple cation electrolyte mixtures on rechargeable Zn–MnO$_2$ alkaline battery. Chem. Mater. **28**, 4536–4545 (2016)

83. Zhang, N., Cheng, F., Liu, J., et al.: Rechargeable aqueous zinc-manganese dioxide batteries with high energy and power densities. Nat. Commun. **8**, 405 (2017)

84. Zhang, L., Chen, L., Zhou, X., et al.: Towards high-voltage aqueous metal-ion batteries beyond 1.5 V: the zinc/zinc hexacyanoferrate system. Adv. Energy. Mater. **5**, 1400930 (2015)

85. Trócoli, R., La Mantia, F.: An aqueous zinc-ion battery based on copper hexacyanoferrate. ChemSusChem **8**, 481–485 (2015)

86. Jayaprakash, N., Das, S.K., Archer, L.A.: The rechargeable aluminum-ion battery. Chem. Commun. **47**, 12610–12612 (2011)

87. Li, Q., Bjerrum, N.J.: Aluminum as anode for energy storage and conversion: a review. J. Power Sources **110**, 1–10 (2002)

88. Zafar, Z.A., Imtiaz, S., Razaq, R., et al.: Cathode materials for rechargeable aluminum batteries: current status and progress. J. Mater. Chem. A **5**, 5646–5660 (2017)

89. He, Y.J., Peng, J.F., Chu, W., et al.: Black mesoporous anatase TiO$_2$ nanoleaves: a high capacity and high rate anode for aqueous Al-ion batteries. J. Mater. Chem. A. **2**, 1721–1731 (2014)

90. Lin, M.C., Gong, M., Lu, B., et al.: An ultrafast rechargeable aluminium-ion battery. Nature **520**, 325–328 (2015)

91. Jung, S.C., Kang, Y.-J., Yoo, D.-J., et al.: Flexible few-layered graphene for the ultrafast rechargeable aluminum-ion battery. J. Phys. Chem. C **120**, 13384–13389 (2016)

92. Chen, H., Guo, F., Liu, Y., et al.: A defect-free principle for advanced graphene cathode of aluminum-ion battery. Adv. Mater. **29**, 1605958 (2017)

93. Takami, N., Koura, N.: Electrochemical behavior of FeS$_2$ cathodes for aluminum secondary cells around 100 °C. J. Electrochem. Soc. **140**, 928–932 (1993)

94. Wang, S., Yu, Z., Tu, J., et al.: A novel aluminum-ion battery: Al/AlCl$_3$-[EMIm]Cl/Ni$_3$S$_2$@Graphene. Adv. Energy Mater. **6**, 1600137 (2016)

95. Wang, S., Jiao, S., Wang, J., et al.: High-performance aluminum-ion battery with CuS@C microsphere composite cathode. ACS Nano **11**, 469–477 (2017)

96. Donahue, F.M., Mancini, S.E., Simonsen, L.: Secondary aluminium-iron (III) chloride batteries with a low temperature molten salt electrolyte. J. Appl. Electrochem. **22**, 230–234 (1992)

97. Zhao, Y., Han, C., Yang, J., et al.: Stable alkali metal ion intercalation compounds as optimized metal oxide nanowire cathodes for lithium batteries. Nano Lett. **15**, 2180–2185 (2015)

98. An, Q., Wei, Q., Zhang, P., et al.: Three-dimensional interconnected vanadium pentoxide nanonetwork cathode for high-rate long-life lithium batteries. Small **11**, 2654–2660 (2015)

99. An, Q., Zhang, P., Wei, Q., et al.: Top-down fabrication of three-dimensional porous V$_2$O$_5$ hierarchical microplates with tunable porosity for improved lithium battery performance. J. Mater. Chem. A. **2**, 3297–3302 (2014)

100. Huie, M.M., Bock, D.C., Takeuchi, E.S., et al.: Cathode materials for magnesium and magnesium-ion based batteries. Coordin. Chem. Rev. **287**, 15–27 (2015)

101. Liu, M., Rong, Z., Malik, R., et al.: Spinel compounds as multivalent battery cathodes: a systematic evaluation based on ab initio calculations. Energy Environ. Sci. **8**, 964–974 (2015)

102. Novák, P., Imhof, R., Haas, O.: Magnesium insertion electrodes for rechargeable nonaqueous batteries—a competitive alternative to lithium? Electrochim. Acta **45**, 351–367 (1999)

103. Novák, P., Scheifele, W., Joho, F., et al.: Electrochemical insertion of magnesium into hydrated vanadium bronzes. J. Electrochem. Soc. **142**, 2544–2550 (1995)

104. Novák, P., Desilvestro, J.: Electrochemical insertion of magnesium in metal oxides and sulfides from aprotic electrolytes. J. Electrochem. Soc. **140**, 140–144 (1993)

105. Le, D.B., Passerini, S., Coustier, F., et al.: Intercalation of polyvalent cations into V$_2$O$_5$ aerogels. Chem. Mater. **10**, 682–684 (1998)

106. Wang, Z., Su, Q., Deng, H.: Single-layered V$_2$O$_5$ a promising cathode material for rechargeable Li and Mg ion batteries: an ab initio study. Phys. Chem. Chem. Phys. **15**, 8705–8709 (2013)

107. Zhou, B., Shi, H., Cao, R., et al.: Theoretical study on the initial stage of a magnesium battery based on a V$_2$O$_5$ cathode. Phys. Chem. Chem. Phys. **16**, 18578–18585 (2014)

108. Gautam, G.S., Canepa, P., Richards, W.D., et al.: Role of structural H$_2$O in intercalation electrodes: the case of Mg in nanocrystalline xerogel-V$_2$O$_5$. Nano Lett. **16**, 2426–2431 (2016)

109. Tepavcevic, S., Liu, Y., Zhou, D., et al.: Nanostructured layered cathode for rechargeable Mg-ion batteries. ACS Nano **9**, 8194–8205 (2015)

110. Lee, S.H., Dileo, R., Marschilok, A.C., et al.: Sol gel based synthesis and electrochemistry of magnesium vanadium oxide: a promising cathode material for secondary magnesium ion batteries. ECS Electrochem. Lett. **3**, A87–A90 (2014)

111. Imamura, D., Miyayama, M., Hibino, M., et al.: Mg intercalation properties into V$_2$O$_5$ gel/carbon composites under high-rate condition. J. Electrochem. Soc. **150**, A753–A758 (2003)

112. Tang, P.E., Sakamoto, J.S., Baudrin, E., et al.: V$_2$O$_5$ aerogel as a versatile host for metal ions. J. Non-Cryst. Solids **350**, 67–72 (2004)

113. Cheng, Y., Shao, Y., Raju, V., et al.: Molecular storage of Mg ions with vanadium oxide nanoclusters. Adv. Funct. Mater. **26**, 3446–3453 (2016)

114. An, Q., Li, Y., Yoo, D.H., et al.: Graphene decorated vanadium oxide nanowire aerogel for long-cycle-life magnesium battery cathodes. Nano. Energy **18**, 265–272 (2015)

115. Du, X., Huang, G., Qin, Y., et al.: Solvothermal synthesis of GO/V$_2$O$_5$ composites as a cathode material for rechargeable magnesium batteries. RSC Adv. **5**, 76352–76355 (2015)

116. Park, S.H., Lee, Y.S., Sun, Y.K.: Synthesis and electrochemical properties of sulfur doped-Li$_x$MnO$_{2-y}$S$_y$ materials for lithium secondary batteries. Electrochem. Commun. **5**, 124–128 (2003)

117. Inamoto, M., Kurihara, H., Yajima, T.: Vanadium pentoxide-based composite synthesized using microwave water plasma for cathode material in rechargeable magnesium batteries. Materials **6**, 4514–4522 (2013)

118. Arthur, T., Kato, K., Germain, J., et al.: Amorphous V$_2$O$_5$–P$_2$O$_5$ as high-voltage cathodes for magnesium batteries. Chem. Commun. **51**, 15657–15660 (2015)

119. Guerra, E.M., Ciuffi, K.J., Oliveira, H.P.: V$_2$O$_5$ xerogel-poly(ethylene oxide) hybrid material: synthesis, characterization, and electrochemical properties. J. Solid State Chem. **179**, 3814–3823 (2006)

120. Chao, D., Xia, X., Liu, J., et al.: A V$_2$O$_5$/conductive-polymer core/shell nanobelt array on three-dimensional graphite foam: a high-rate, ultrastable, and freestanding cathode for lithium-ion batteries. Adv. Mater. **26**, 5794–5800 (2014)

121. Huguenin, F., Torresi, R.M.: Investigation of the electrical and electrochemical properties of nanocomposites from V$_2$O$_5$, polypyrrole, and polyaniline. J. Phys. Chem. C **112**, 2202–2209 (2008)

122. Reddy, C.V.S., Wei, J., Quan-Tao, Z., et al.: Cathodic performance of (V$_2$O$_5$+PEG) nanobelts for Li ion rechargeable battery. J. Power Sources **166**, 244–249 (2007)

123. Shao, L., Jeon, J.W., Lutkenhaus, J.: Porous polyaniline nanofiber/vanadium pentoxide layer-by-layer electrodes for energy storage. J. Mater. Chem. A **1**, 7648–7656 (2013)

124. Perera, S.D., Archer, R.B., Damin, C.A., et al.: Controlling inter-layer interactions in vanadium pentoxide-poly(ethylene oxide) nanocomposites for enhanced magnesium-ion charge transport and storage. J. Power Sources **343**, 580–591 (2017)

125. Kulish, V.V., Manzhos, S.: Comparison of Li, Na, Mg and Al-ion insertion in vanadium pentoxides and vanadium dioxides. RSC Adv. **7**, 18643–18649 (2017)

126. Niu, C., Meng, J., Han, C., et al.: VO_2 nanowires assembled into hollow microspheres for high-rate and long-life lithium batteries. Nano Lett. **14**, 2873–2878 (2014)

127. Luo, T., Liu, Y., Su, H., et al.: Nanostructured-VO_2(B): a high-capacity magnesium-ion cathode and its electrochemical reaction mechanism. Electrochim. Acta **260**, 805–813 (2018)

128. Won, J.M., Ko, Y.N., Lee, J.K., et al.: Superior electrochemical properties of rutile VO_2-carbon composite microspheres as a promising anode material for lithium ion batteries. Electrochim. Acta **156**, 179–187 (2015)

129. Pei, C., Xiong, F., Sheng, J., et al.: VO_2 nanoflakes as the cathode material of hybrid magnesium–lithium-ion batteries with high energy density. ACS. Appl. Mater. Inter. **9**, 17060–17066 (2017)

130. Jiao, L., Yuan, H., Si, Y., et al.: Electrochemical insertion of magnesium in open-ended vanadium oxide nanotubes. J. Power Sources **156**, 673–676 (2006)

131. Kim, R.H., Kim, J.S., Kim, H.J., et al.: Highly reduced VO_x nanotube cathode materials with ultra-high capacity for magnesium ion batteries. J. Mater. Chem. A **2**, 20636–20641 (2014)

132. Jiao, L., Yuan, H., Wang, Y., et al.: Mg intercalation properties into open-ended vanadium oxide nanotubes. Electrochem. Commun. **7**, 431–436 (2005)

133. Patzke, G.R., Krumeich, F., Nesper, R.: Oxidic nanotubes and nanorods-anisotropic modules for a future nanotechnology. Angew. Chem. Int. Ed. **41**, 2446–2461 (2002)

134. Novák, P., Scheifele, W., Haas, O.: Magnesium insertion batteries-an alternative to lithium? J. Power Sources **54**, 479–482 (1995)

135. Rashad, M., Zhang, H., Asif, M., et al.: Low cost room temperature synthesis of $NaV_3O_8.1.69H_2O$ nanobelts for Mg batteries. ACS Appl. Mater. Interfaces **10**, 4757–4766 (2018)

136. Cabello, M., Nacimiento, F., Alcántara, R., et al.: Nanobelts of beta-sodium vanadate as electrode for magnesium and dual magnesium-sodium batteries. J. Electrochem. Soc. **163**, A2781–A2790 (2016)

137. Chen, B., Laverock, J., Newby, D., et al.: Electronic structure of β-$Na_xV_2O_5$ ($x \approx 0.33$) polycrystalline films: growth, spectroscopy, and theory. J. Phys. Chem. C **118**, 1081–1094 (2014)

138. Delmas, C., Nadiri, A., Soubeyroux, J.L.: The nasicon-type titanium phosphates $ATi_2(PO_4)_3$ (A = Li, Na) as electrode materials. Solid State Ion. **28–30**((Part 1)), 419–423 (1988)

139. Ong, S.P., Chevrier, V.L., Hautier, G., et al.: Voltage, stability and diffusion barrier differences between sodium-ion and lithium-ion intercalation materials. Energy Environ. Sci. **4**, 3680–3688 (2011)

140. Shi, J.J., Yin, G.Q., Jing, L.M., et al.: Lithium and sodium diffusion in solid electrolyte materials of $AM_2(PO_4)_3$(A = Li, Na, M = Ti, Sn and Zr). Int. J. Mod. Phys. B **28**, 1450176 (2014)

141. Kang, J., Chung, H., Doh, C., et al.: Integrated study of first principles calculations and experimental measurements for Li-ionic conductivity in Al-doped solid-state $LiGe_2(PO_4)_3$ electrolyte. J. Power Sources **293**, 11–16 (2015)

142. Goodenough, J.B., Hong, Y.P., Kafalas, J.A.: Fast Na^+-ion transport in skeleton structures. Mater. Res. Bull. **11**, 203–220 (1976)

143. Makino, K., Katayama, Y., Miura, T., et al.: Electrochemical insertion of magnesium to $Mg_{0.5}Ti_2(PO_4)_3$. J. Power Sources **99**, 66–69 (2001)

144. Huang, Z.D., Masese, T., Orikasa, Y., et al.: Vanadium phosphate as a promising high-voltage magnesium ion (de)-intercalation cathode host. RSC Adv. **5**, 8598–8603 (2015)

145. Kim, J., Yoo, J.K., Jung, Y.S., et al.: $Li_3V_2(PO_4)_3$/conducting polymer as a high power 4 V-class lithium battery electrode. Adv. Energy Mater. **3**, 1004–1007 (2013)

146. Liu, H., Gao, P., Fang, J., et al.: $Li_3V_2(PO_4)_3$/graphene nanocomposites as cathode material for lithium ion batteries. Chem. Commun. **47**, 9110–9112 (2011)

147. Muldoon, J., Bucur, C.B., Oliver, A.G., et al.: Electrolyte roadblocks to a magnesium rechargeable battery. Energy Environ. Sci. **5**, 5941–5950 (2012)

148. Canepa, P., Gautam, G.S., Malik, R., et al.: Understanding the initial stages of reversible Mg deposition and stripping in inorganic nonaqueous electrolytes. Chem. Mater. **27**, 3317–3325 (2015)

149. Canepa, P., Jayaraman, S., Cheng, L., et al.: Elucidating the structure of the magnesium aluminum chloride complex electrolyte for magnesium-ion batteries. Energy Environ. Sci. **8**, 3718–3730 (2015)

150. Cabello, M., Alcántara, R., Nacimiento, F., et al.: $Na_3V_2(PO_4)_3$ as electrode material for rechargeable magnesium batteries: a case of sodium-magnesium hybrid battery. Electrochim. Acta **246**, 908–913 (2017)

151. Li, Y., An, Q., Cheng, Y., et al.: A high-voltage rechargeable magnesium-sodium hybrid battery. Nano Energy **34**, 188–194 (2017)

152. Zeng, J., Yang, Y., Lai, S., et al.: A promising high-voltage cathode material based on mesoporous $Na_3V_2(PO_4)_3$/C for rechargeable magnesium batteries. Chem-Eur. J. **23**, 16898–16905 (2017)

153. Prosini, P.P., Lisi, M., Zane, D., et al.: Determination of the chemical diffusion coefficient of lithium in $LiFePO_4$. Solid State Ion. **148**, 45–51 (2002)

154. Rui, X.H., Ding, N., Liu, J., et al.: Analysis of the chemical diffusion coefficient of lithium ions in $Li_3V_2(PO_4)_3$ cathode material. Electrochim. Acta **55**, 2384–2390 (2010)

155. Böckenfeld, N., Balducci, A.: Determination of sodium ion diffusion coefficients in sodium vanadium phosphate. J. Solid State Electrochem. **18**, 959–964 (2014)

156. Kaveevivitchai, W., Jacobson, A.J.: High capacity rechargeable magnesium-ion batteries based on a microporous molybdenum–vanadium oxide cathode. Chem. Mater. **28**, 4593–4601 (2016)

157. Miao, X., Chen, Z., Wang, N., et al.: Electrospun V_2MoO_8 as a cathode material for rechargeable batteries with Mg metal anode. Nano Energy **34**, 26–35 (2017)

158. Cho, J.H., Aykol, M., Kim, S., et al.: Controlling the intercalation chemistry to design high-performance dual-salt hybrid rechargeable batteries. J. Am. Chem. Soc. **136**, 16116–16119 (2014)

159. Gao, T., Han, F., Zhu, Y., et al.: Hybrid Mg^{2+}/Li^+ battery with long cycle life and high rate capability. Adv. Energy Mater. **5**, 1401507 (2015)

160. Zhang, Z., Xu, H., Cui, Z., et al.: High energy density hybrid Mg^{2+}/Li^+ battery with superior ultra-low temperature performance. J. Mater. Chem. A **4**, 2277–2285 (2016)

161. Minella, C.B., Gao, P., Zhao-Karger, Z., et al.: Interlayer-expanded vanadium oxychloride as an electrode material for magnesium-based batteries. ChemElectroChem **4**, 738–745 (2017)

162. Hannah, D.C., Gautam, G.S., Canepa, P., et al.: Magnesium ion mobility in post-spinels accessible at ambient pressure. Chem. Commun. **53**, 5171–5174 (2017)

163. Ling, C., Mizuno, F.: Phase stability of post-spinel compound AMn_2O_4 (A = Li, Na, or Mg) and its application as a rechargeable battery cathode. Chem. Mater. **25**, 3062–3071 (2013)

164. Sun, X., Blanc, L., Nolis, G.M., et al.: $NaV_{1.25}Ti_{0.75}O_4$: a potential post spinel cathode material for Mg batteries. Chem. Mater. **30**, 121–128 (2018)

165. Yan, M., He, P., Chen, Y., et al.: Water-lubricated intercalation in $V_2O_5 \cdot H_2O$ for high-capacity and high-rate aqueous rechargeable zinc batteries. Adv. Mater. **30**, 1703725 (2018)

166. Senguttuvan, P., Han, S.D., Kim, S., et al.: A high power rechargeable nonaqueous multivalent Zn/V_2O_5 battery. Adv. Energy Mater. **6**, 1600826 (2016)

167. Kundu, D., Adams, B.D., Ort, V.D., et al.: A high-capacity and long-life aqueous rechargeable zinc battery using a metal oxide intercalation cathode. Nat. Energy **1**, 16119 (2016)

168. Baghbanzadeh, M., Carbone, L., Cozzoli, P.D., et al.: Microwave-assisted synthesis of colloidal inorganic nanocrystals. Angew. Chem. Int. Ed. **50**, 11312–11359 (2011)

169. He, P., Zhang, G., Liao, X., et al.: Sodium ion stabilized vanadium oxide nanowire cathode for high-performance zinc-ion batteries. Adv. Energy. Mater **8**, 1702463 (2018)

170. Xia, C., Guo, J., Lei, Y., et al.: Rechargeable aqueous zinc-ion battery based on porous framework zinc pyrovanadate intercalation cathode. Adv. Mater. **30**, 1705580 (2018)

171. Alfaruqi, M.H., Mathew, V., Song, J., et al.: Electrochemical zinc intercalation in lithium vanadium oxide: a high-capacity zinc-ion battery cathode. Chem. Mater. **29**, 1684–1694 (2017)

172. Tang, H., Xu, N., Pei, C., et al.: $H_2V_3O_8$ nanowires as high-capacity cathode materials for magnesium-based battery. ACS. Appl. Mater. Interfaces **9**, 28667–28673 (2017)

173. He, P., Quan, Y., Xu, X., et al.: High-performance aqueous zinc-ion battery based on layered $H_2V_3O_8$ nanowire cathode. Small **13**, 1702551 (2017)

174. Li, H., He, P., Wang, Y., et al.: High-surface vanadium oxides with large capacities for lithium-ion batteries: from hydrated aerogel to nanocrystalline $VO_2(B)$, V_6O_{13} and V_2O_5. J. Mater. Chem. A **21**, 10999–11009 (2011)

175. Sarkar, S., Bhowmik, A., Pan, J., et al.: Preparation, structure study and electrochemistry of layered $H_2V_3O_8$ materials: high capacity lithium-ion battery cathode. J. Power Sources **329**, 179–189 (2016)

176. Su, D., Wang, G.: Single-crystalline bilayered V_2O_5 nanobelts for high-capacity sodium-ion batteries. ACS Nano **7**, 11218–11226 (2013)

177. Li, G., Yang, Z., Jiang, Y., et al.: Towards polyvalent ion batteries: a zinc-ion battery based on NASICON structured $Na_3V_2(PO_4)_3$. Nano Energy **25**, 211–217 (2016)

178. Wang, D., Wei, Q., Sheng, J., et al.: Flexible additive free $H_2V_3O_8$ nanowire membrane as cathode for sodium ion batteries. Phys. Chem. Chem. Phys. **18**, 12074–12079 (2016)

179. Mason, C.W., Lange, F.: Aqueous ion battery systems using sodium vanadium phosphate stabilized by titanium substitution. ECS Electrochem. Lett. **4**, A79–A82 (2015)

180. He, P., Yan, M., Zhang, G., et al.: Layered VS_2 nanosheet-based aqueous Zn ion battery cathode. Adv. Energy Mater. **7**, 1601920 (2017)

181. Jo, J.H., Sun, Y.K., Myung, S.T.: Hollandite-type Al-doped $VO_{1.52}(OH)_{0.77}$ as a zinc ion insertion host material. J. Mater. Chem. A **5**, 8367–8375 (2017)

182. Xu, H.T., Zhang, H., Liu, L., et al.: Fabricating hexagonal Al-doped $LiCoO_2$ nanomeshes based on crystal-mismatch strategy for ultrafast lithium storage. ACS Appl. Mater. Interfaces **7**, 20979–20986 (2015)

183. Reed, L.D., Menke, E.: The roles of V_2O_5 and stainless steel in rechargeable Al-ion batteries. J. Electrochem. Soc. **160**, A915–A917 (2013)

184. Wang, H., Bai, Y., Chen, S., et al.: Binder-free V_2O_5 cathode for greener rechargeable aluminum battery. ACS Appl. Mater. Interfaces **7**, 80–84 (2015)

185. Gu, S., Wang, H., Wu, C., et al.: Confirming reversible Al^{3+} storage mechanism through intercalation of Al^{3+} into V_2O_5 nanowires in a rechargeable aluminum battery. Energy Storage Mater. **6**, 9–17 (2017)

186. Chiku, M., Takeda, H., Matsumura, S., et al.: Amorphous vanadium oxide/carbon composite positive electrode for rechargeable aluminum battery. ACS Appl. Mater. Interfaces **7**, 24385–24389 (2015)

187. Endres, F.: Physical chemistry of ionic liquids. Phys. Chem. Chem. Phys. **12**, 1648 (2010)

188. Koketsu, T., Ma, J., Morgan, B.J., et al.: Reversible magnesium and aluminium ions insertion in cation-deficient anatase TiO_2. Nat. Mater. **16**, 1142–1148 (2017)

189. Wang, H., Gu, S., Bai, Y., et al.: High-voltage and noncorrosive ionic liquid electrolyte used in rechargeable aluminum battery. ACS. Appl. Mater. Interfaces **8**, 27444–27448 (2016)

190. Wang, H., Gu, S., Bai, Y., et al.: Anion-effects on electrochemical properties of ionic liquid electrolytes for rechargeable aluminum batteries. J. Mater. Chem. A **3**, 22677–22686 (2015)

191. González, J.R., Nacimiento, F., Cabello, M., et al.: Reversible intercalation of aluminium into vanadium pentoxide xerogel for aqueous rechargeable batteries. RSC Adv. **6**, 62157–62164 (2016)

192. Wang, W., Jiang, B., Xiong, W., et al.: A new cathode material for super-valent battery based on aluminium ion intercalation and deintercalation. Sci. Rep. **3**, 3383 (2013)

193. Zhang, C., Song, H., Liu, C., et al.: Fast and reversible Li ion insertion in carbon-encapsulated Li_3VO_4 as anode for lithium-ion battery. Adv. Funct. Mater. **25**, 3497–3504 (2015)

194. Li, Q., Wei, Q., Sheng, J., et al.: Mesoporous Li_3VO_4/C submicron-ellipsoids supported on reduced graphene oxide as practical anode for high-power lithium-ion batteries. Adv. Sci. **2**, 1500284 (2015)

195. Jiang, J., Li, H., Huang, J., et al.: Investigation of the reversible intercalation/deintercalation of Al into the novel Li_3VO_4@C microsphere composite cathode material for aluminum-ion batteries. ACS. Appl. Mater. Interfaces **9**, 28486–28494 (2017)

196. Nacimiento, F., Cabello, M., Alcántara, R., et al.: NASICON-type $Na_3V_2(PO_4)_3$ as a new positive electrode material for rechargeable aluminium battery. Electrochim. Acta **260**, 798–804 (2017)

197. Sun, X.G., Zhang, Z., Guan, H.Y., et al.: A sodium-aluminum hybrid battery. J. Mater. Chem. A **5**, 6589–6596 (2017)

198. Anasori, B., Lukatskaya, M.R., Gogotsi, Y.: 2D metal carbides and nitrides (MXenes) for energy storage. Nat. Rev. Mater. **2**, 16098 (2017)

199. Vahidmohammadi, A., Hadjikhani, A., Shahbazmohamadi, S., et al.: Two-dimensional vanadium carbide (MXene) as a high capacity cathode material for rechargeable aluminum batteries. ACS Nano **11**, 11135–11144 (2017)

200. Zhang, X., Wang, S., Tu, J., et al.: Flower-like vanadium sulfide/reduced graphene oxide composite: an energy storage material for aluminum-ion batteries. ChemSusChem **11**, 709–715 (2018)
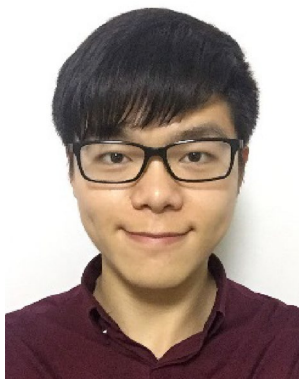
Han Tang received his B.S. degree in Department of Materials Science and Engineering from Hubei University of Technology in 2016. He is currently working toward the Ph.D. degree at Wuhan University of Technology. His current research involves the nanomaterials achieving high energy density and power density for rechargeable multivalent batteries.

Cunyuan Pei received his B.S. degree in Department of Materials Science and Engineering from Hebei University of Architecture in 2014. He is currently working toward the Ph.D. degree and focuses on nanomaterials and electrolytes for magnesium ion battery.
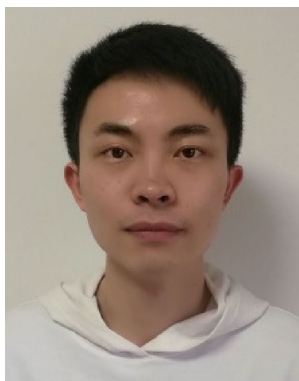
Zhuo Peng received his B.S. degree in Department of Materials Science and Engineering from Hubei University in 2016. He is currently working toward the master degree in Material Science and Engineering at Wuhan University of Technology. His current research focuses on the energy storage materials and devices.

Qinyou An is Associate Professor of Materials Science and Engineering at Wuhan University of Technology (WUT). He received his Ph.D. degree from WUT in 2014. He carried out his postdoctoral research in the laboratory of Prof. Yan Yao at the University of Houston in 2014–2015. Currently, his research interest includes energy storage materials and devices.
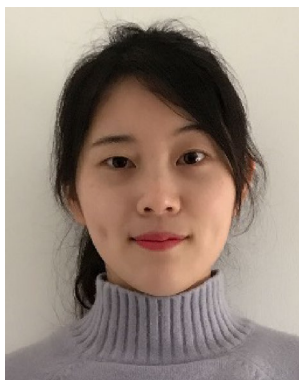
Lu Wu is currently working toward the master degree in Material Science and Engineering at Wuhan University of Technology. Her current research focuses on electrode materials for emerging energy storage devices.

Liqiang Mai is Chair Professor of Materials Science and Engineering at Wuhan University of Technology (WUT). He is Chang Jiang Scholar Professor of the Ministry of Education, China, and the winner of the National Natural Science Fund for Distinguished Young Scholars. He received his Ph.D. degree from WUT in 2004. He carried out his postdoctoral research in Prof. Zhonglin Wang's group at Georgia Institute of Technology in 2006–2007. He worked as advanced research scholar in the laboratory of Prof. Charles M. Lieber at Harvard University in 2008–2011 and the laboratory of Prof. Peidong Yang at University of California, Berkeley in 2017. His current research interests focus on new nanomaterials for electrochemical energy storage and micro/nano energy devices.

Fangyu Xiong received his B.S. degree in Material Physics and Chemistry from Wuhan University of Technology in 2016. He is currently working toward the Ph.D. degree and his current research interests focuses on electrode materials for emerging energy storage devices.